Anthropogenic beach deformations

Characterizing anthropogenic beach changes using laser scan and video data

D.A.J. van Dieren

Bachelor Thesis

Faculty of Civil Engineering and Geosciences
Supervisors Mieke Kuschnerus, Sander Vos, Roderik Lindenbergh

June 2022

Abstract

Understanding coastal dynamics is highly important to ensure coastal protection. However, current research focuses mainly on understanding natural processes and often lacks consideration of anthropogenic influences. Anthropogenic deformations should be taken into account to prevent misinterpretation of natural deformations and to recognize coastal safety threats caused by humans.

This thesis focuses on finding anthropogenic beach deformations in the period February 20 to April 26, 2020 in Noordwijk, the Netherlands. The anthropogenic beach deformations are characterized in laser data and validated in video data. The characterization in the laser data is done using a decision tree that filters out deformations with non-anthropogenic causes. All deformations left are marked as anthropogenic deformations, which was the case for 30 deformations. Validation in the video data shows 16 of these deformations have an anthropogenic cause, as a bulldozer is seen in the area of deformation. The methodology to filter out anthropogenic deformations is proven successfull and this thesis lays a basis for further research on anthropogenic influences in beach areas.

Contents

1 Introduction **1**
- 1.1 Problem statement . . . 1
- 1.2 Objective and scope . . . 1
- 1.3 Research question . . . 1
- 1.4 Thesis overview . . . 2

2 Literature Review on beach deformation causes and measurements **3**
- 2.1 Natural sediment transport on sandy beaches . . . 3
  - 2.1.1 Marine processes . . . 3
  - 2.1.2 Aeolian processes . . . 4
- 2.2 Anthropogenic influences on beaches . . . 5
- 2.3 Laser data . . . 6
  - 2.3.1 Working principle . . . 6
  - 2.3.2 Limitations . . . 7
- 2.4 Video data . . . 8
  - 2.4.1 Working principle . . . 8
  - 2.4.2 Limitations . . . 8
- 2.5 Related work . . . 8

3 Characteristics of the data **11**
- 3.1 Site Description . . . 11
- 3.2 Laser instrument . . . 12
- 3.3 Video instrument . . . 13
- 3.4 Dates and data gaps . . . 13

4 Change detection analysis **15**
- 4.1 Pre-processing . . . 15
  - 4.1.1 Data selection . . . 15
  - 4.1.2 Apply transformations . . . 15
  - 4.1.3 Clip to the area of interest . . . 17
  - 4.1.4 Gridding . . . 17
  - 4.1.5 Check on incomplete point clouds . . . 18
- 4.2 Change detection in laser data . . . 19
  - 4.2.1 Visual analysis . . . 19
  - 4.2.2 Decision tree . . . 19
- 4.3 Validation in video data . . . 20

5 Results **23**
- 5.1 Visual analysis of laser data . . . 23
- 5.2 Apply decision tree to laser data . . . 24
- 5.3 Validation of anthropogenic causes in video data . . . 26
  - 5.3.1 Expected anthropogenic cause found . . . 27
  - 5.3.2 Expected anthropogenic cause not found . . . 27
- 5.4 Additional results video data . . . 32
  - 5.4.1 Unexpected anthropogenic deformations . . . 32
  - 5.4.2 Vehicles and sand waves check . . . 32
  - 5.4.3 Image quality . . . 34

6 Discussion **35**
6.1 Criteria of the decision tree . . . 35
6.2 Other deformation causes . . . 36
6.3 Improvements to the decision tree . . . 36
6.4 Limitations of the laser data . . . 37
6.5 Limitations of the video data . . . 37

7 Conclusion and recommendations **39**
7.1 Conclusion . . . 39
7.2 Recommendations . . . 40

A Images resulting from video validation **43**
A.1 Expected and found . . . 43
A.2 Expected, not found . . . 49
A.3 Unexpected and found . . . 53
A.4 Check sand waves and vehicles . . . 55
A.5 Low image quality . . . 57

B Python script **59**

1 Introduction

In this chapter, the problem statement is given in section 1.1. The objective and scope of this thesis can be found in section 1.2. Section 1.3 contains the research question and section 1.4 gives an overview of the thesis.

1.1. Problem statement

Coastal protection has always been crucial in The Netherlands, where considerable areas lie below sea level. Currently, the global mean sea level is rising due to climate change and is expected to rise by 30-110 cm towards the end of this century (IPCC, 2021). The urge for thorough knowledge of coastal processes increases even more, as floods should be prevented even with rising sea levels.

To predict the impact of current and future developments, understanding the coastal dynamics is highly important. Many natural processes, like aeolian sand transport or marine influences on morphology, have been examined in existing research (Anders et al., 2019; Hage et al., 2018; Jin et al., 2021; Strypsteen, 2019; Vos et al., 2020). Still, most of this research does not consider anthropogenic influences on the beach morphology, whilst there are examples of human interventions on beaches, which influence the coastal dynamics (Bosveld, 2020; Lazarus and Goldstein, 2019). Not considering anthropogenic influences has a two-fold effect. First of all, morphological analyses that consider only natural deformation causes are misinterpreted, as they might in fact be influenced by anthropogenic interventions. Secondly, anthropogenic deformations might be as important as natural deformations to coastal protection (Lazarus and Goldstein, 2019). Thus, it is important to understand the influence of anthropogenic beach deformations.

1.2. Objective and scope

This thesis seeks to characterize anthropogenic beach deformations in Terrestrial Laser Scanning data. Validation of anthropogenic interventions will be done using video data. The video data is available in the period from February 21, 2020 until April 26, 2020 and the site is located in Noordwijk, The Netherlands. Ideally, natural and anthropogenic beach deformations can be distinguished clearly in the laser data at the end of this thesis. In reality, however, this might not be fully possible due to limitations of the video and laser data.

1.3. Research question

In order to find anthropogenic deformations, the following research question is used:

> *How can anthropogenic beach deformations be characterized in laser data, using video data as validation?*

The research question is divided into several sub-questions. First of all, possible deformation causes are examined using sub-question 1: '*What are main causes of beach deformations and what characteristics do these types of deformations have?*'. The second sub-question '*How is the laser and*

video data obtained and what are limitations of the laser and video data?' focuses on the type of data and its limitations. The laser data is linked to anthropogenic causes in sub-question 3: '*How can the laser data be used to link deformations to human causes?*'. In sub-question 4, the deformation causes are validated in the video data: '*Which deformations of the laser data are linked to human causes, using video data?*'.

1.4. Thesis overview

In chapter 2, a theoretical background is given on deformation causes and laser and video data. In addition, an overview of related work is given. Chapter 3 contains information on the used laser and video instruments, together with a site description. In chapter 4, the change detection analysis is explained and the results of the analysis are given in chapter 5. The results are discussed in chapter 6. The conclusion and recommendations can be found in chapter 7.

2

Literature Review on beach deformation causes and measurements

This chapter contains information from literature. Information on naturally caused sand transport on beaches is given in section 2.1. Section 2.2 elaborates on anthropogenic caused beach deformations. In section 2.3 and 2.4, the working principle and limitations of the laser and video data are explained. Section 2.5 discusses related work.

2.1. Natural sediment transport on sandy beaches

The site in Noordwijk is a beach-dune system with a sandy beach. A beach-dune system can be divided into several areas, see figure 2.1. The distinction between these five areas is based on morphological changes at the Belgian coast (Houthuys, 2012). The *bed* and *foreshore area* are below the water level. In the foreshore area, the water depth decreases and the waves break. The *intertidal beach* is the area that is flooded during high tide and which is not flooded during low tide. The *dry beach* is the unflooded beach area of the beach-dune system. Only in extreme cases, such as storms, this area is flooded. The *coastal dune area* is the highest part of the beach-dune system. The dunes are formed by the sediment transported by wind and vegetation holding the sediment.

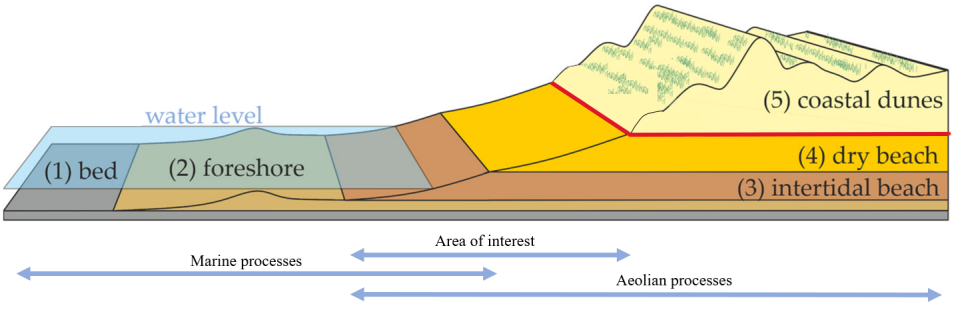

Figure 2.1: An overview of the beach-dune system, divided into five areas (adapted from (Eichmanns and Schüttrumpf, 2021))

This thesis focuses on the intertidal beach and the dry beach areas, see Figure 2.1. These areas are not only subject to anthropogenic deformations. Naturally caused deformations occur here as well and can be subdivided into marine and aeolian processes. Section 2.1.1 and 2.1.2 elaborate on the main forces which describe the natural deformations.

2.1.1. Marine processes

The marine processes describe the dynamic interplay between the sea and the sandy beach. As a result, erosion and sedimentation occur along the coastline. These processes take place in the intertidal area and not on the dry beach area, as the water level remains below the dry beach, see

Figure 2.1. Important parameters in these processes are the wave height, water depth, flow velocity, and sand particle characteristics, such as size, density, and shape.

On sandy beaches, the water forms intertidal bars. Those intertidal bars are piles of sand, stretching along the coast. These bars are located in the intertidal area. Figure 2.2 shows the location of an intertidal bar, together with different water levels during a tide.

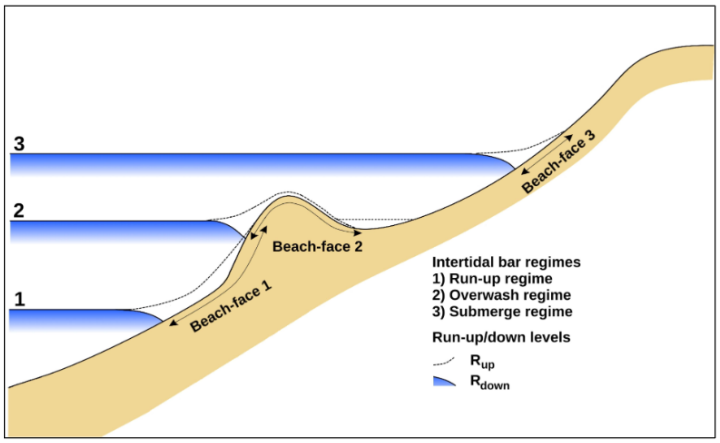

Figure 2.2: Visualisation of an intertidal bar with the water levels during low (1) and high (3) tide and a moment in between (2) (Vos et al., 2020)

Vos et al. (2020) examined the behaviour of intertidal bars at the Dutch coast. From the analysis of the beach at Kijkduin follow some variables which might later become useful to filter out natural deformations. For a tidal period in the construction phase, the maximum growth in height was about a meter, the maximum observed erosion/sedimentation flux S was 0.2 m^3 and the maximum total sediment transport Q was 1.3 m^3/m. In the destructive phase, the maximum flux S was 0.4 m^3/m and the maximum total sediment transport Q was 0.4 m^3.

2.1.2. Aeolian processes

Aeolian sediment transport is sediment transport caused by wind. Important parameters that determine the aeolian sand transport are wind speed, moisture content of the sand, and characteristics of the sand particles, such as grain size, shape, and density.

Sand waves

Sand waves are sand strips formed by the wind. The wind-blown sand has a lower moisture content and has therefore a lighter colour, giving visual contrast. This visual contrast can be used to recognize sand waves in video data (Hage et al., 2018).

Boomaars (2022) found a maximum height difference of 15 cm between the top and the bottom of sand waves in Noordwijk. According to other literature, the sand waves become dunes when the height becomes of the order of decimeters to centimeters. However, the sand waves are often destroyed before reaching those heights (Hage et al., 2018). A third indication of the height of sand waves is found in Schreijer (2021). Figure 2.3 shows the height difference over a period where sand waves arose. The order of elevation can be derived from the figure and ranges at least from -0.20 m to +0.20 m.

More aeolian sand transport occurs when the wind direction is parallel to the coast, compared to a wind direction normal to the coast (Boomaars, 2022; Strypsteen, 2019).

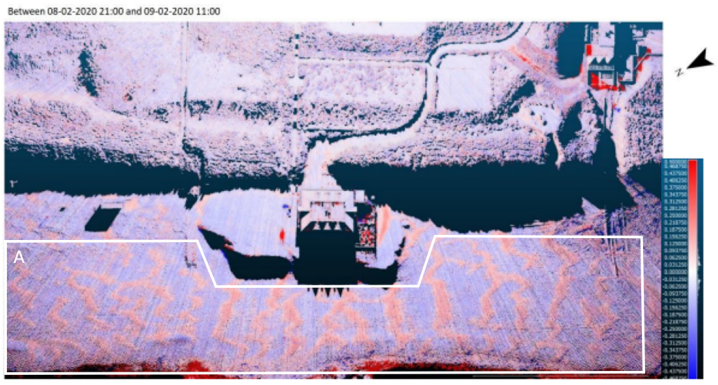

Figure 2.3: The height differences of the beach between 8-2-2020 21:00 and 9-2-2020 11:00 (adapted from Schreijer, 2021). Red indicates an increase in height, blue indicates a decrease in height. Sand waves are clearly visible in area A.

Dune growth

Aside from sand waves, aeolian sand transport can also be from the beach to the coastal dune area. The Belgian beach-dune system is similar to the Dutch coast and has a dune growth of 0-12.3 $m^3/m/year$ and an average of 6.2 $m^3/m/year$ (Strypsteen, 2019). At the Dutch coast, dunes increase with 0–40 $m3/m/year$ (de Vries et al., 2012). These quantities can therefore be used as a rough estimation of natural dune growth due to wind.

2.2. Anthropogenic influences on beaches

Anthropogenic beach deformations are due to various human activities. This thesis focuses on changes caused by heavy equipment, such as bulldozers. Other human activities forming beach deformations are caused by buildings or the temporary presence of humans on the beach.

Buildings

The construction and presence of structures placed by humans can cause beach deformations. When buildings, containers, or boulevards are placed on the beach, the beach deforms during the lifespan, because the shape of the structure influences the aeolian sand transport. The direction of the wind around a building is visualised in Figure 2.4. An analysis of Bosveld (2020) shows that morphological change is the largest at the lee side of a structure, where the height changes between +0.5 and -0.5 m in a period of three months.

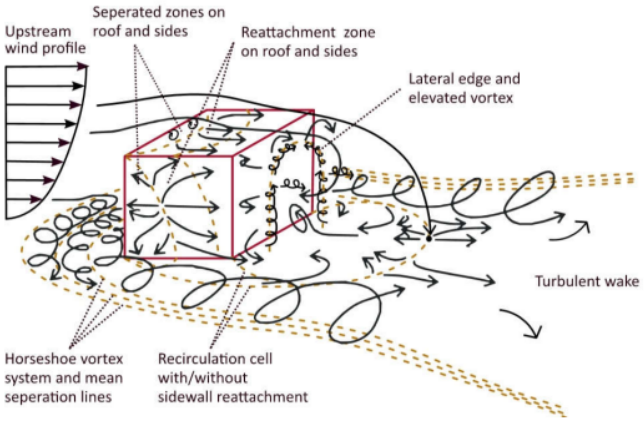

Figure 2.4: The working principle of wind around a structure.

Small-scale deformations

In Noordwijk, tourism is a considerable source of income. In 2013, 25% of all positions of employment in Noordwijk were in the tourism sector and 13% of all commercial buildings in Noordwijk were linked

to tourism. These two numbers are notably higher than many other Dutch municipalities (CBR, 2014). Therefore, many tourists can be expected at this part of the Dutch coastline. These deformations are expected to be small and have less influence on the point cloud data compared to heavy equipment. This thesis focuses more on large-scale deformations caused by heavy equipment than on these small-scale deformations.

Heavy equipment
Heavy equipment, like bulldozers, can be present at the beach. In literature, cases of such deformation causes are found, especially in major storm events (Lazarus and Goldstein, 2019). This thesis focuses on finding deformations caused by heavy equipment in the laser data of Noordwijk. In Noordwijk, bulldozers can be used to clear paths and other areas around the beach pavilion. In addition, heavy equipment can create a platform of sand around the terrace to protect the terrace against high water.

2.3. Laser data

Knowledge of the principle of the laser instrument is helpful to interpret the laser data correctly. In this section, the working principle of the laser instrument is explained, followed by limitations of the laser data.

2.3.1. Working principle

Before the working principle is explained in detail, some terminology is explained. First of all, laser is the abbreviation for Light Amplification by Stimulated Emission of Radiation (Tiberius et al., 2021). In the case of LiDAR (Light Detection and Ranging), laser data is used to create a cloud of 3D points of a certain area (Eitel et al., 2016). Terrestrial Laser Scanning (TLS) is used for laser scanning from a fixed position on the ground. All three terms can be used in this case, as TLS uses LiDAR, and LiDAR uses a laser.

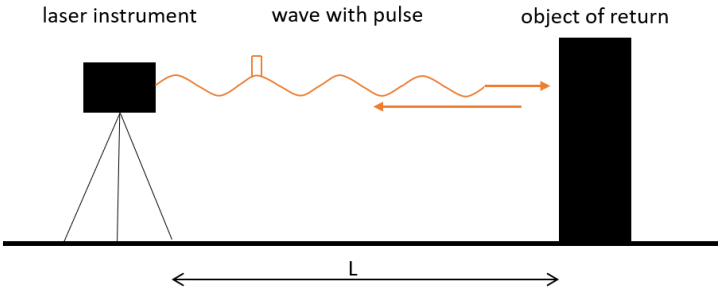

Figure 2.5: The working principle of a laser scanner using a pulse.

A laser device emits waves of a single frequency, with wavelengths ranging between 500 nm (visible light) and 1500 nm (short-wavelength infrared). A signal, typically a short pulse, is added to the wave. The pulse is transmitted towards an object, is reflected by that object, and travels back to the measurement device. These steps are visualised in Figure 2.5. A strongly reflecting surface reflects the waves and the pulse (almost) entirely in the direction of the measuring device. Other surfaces, like water bodies, reflect little to nothing of the waves and the pulse (Vosselman and Maas, 2010).

The measuring device measures the time between the emission and receiving of the pulse, which is called the signal travel-time $\Delta\tau$ (Tiberius et al., 2021). As the waves propagate with the speed of light c, the distance between the object and the measurement device (Δl) can be determined, using:

$$\Delta l = \frac{c \cdot \Delta\tau}{2}$$

Another way of measuring the distance between the measurement device and the object is by using the phase difference between the emitted and the received wave, instead of using a pulse (Tiberius et al., 2021). However, this method does not apply to this thesis and is therefore not discussed extensively here.

Thus far, only single measurements have been explained, whilst point clouds may contain millions of points. A terrestrial laser scanner, having a set position on the ground, is used in Noordwijk. As shown in Figure 2.6, this station can move around the horizontal and the vertical axis. For a horizontal angle, many signals are transmitted around the vertical axis by using a mirror. The signals are received again, creating points of a slice of the area. Next, the horizontal angle changes slightly and the next slice of points is created. This process continues until the whole area is covered (Vosselman and Maas, 2010).

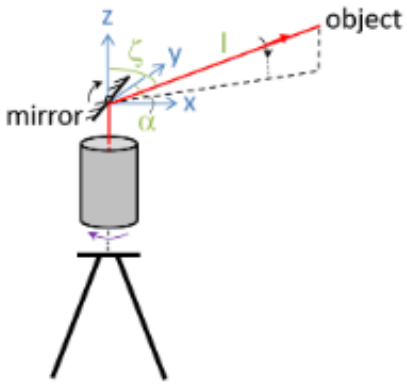

Figure 2.6: The laser scanner measures incoming waves with a horizontal and vertical angle (Tiberius et al., 2021).

2.3.2. Limitations

The laser data is negatively impacted by various factors. These factors are explained below.

Laser shadow

The laser instrument measures the distance between the laser and the first object a radiation beam encounters. However, some areas become invisible as the radiation beam is reflected earlier, due to differences in elevation. This is visualised in Figure 2.7. Thus, areas behind high objects cannot be scanned. Examples of high objects in this thesis are dunes, piles of sand and buildings. These objects have a laser shadow area in the point clouds, where no data is available.

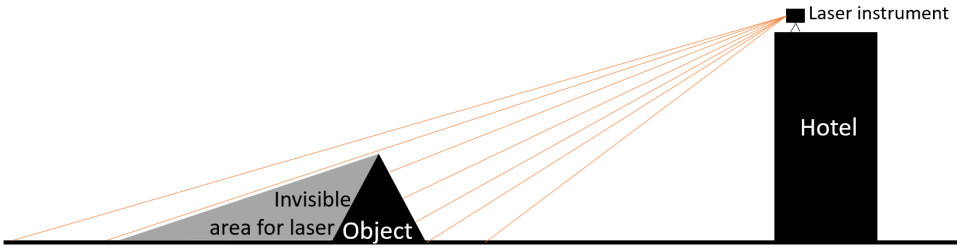

Figure 2.7: Areas can become invisible if a higher object is placed between the laser instrument and the area.

Wind

The inclination of the laser instrument is correlated to wind data. So, at higher wind speeds, the instrument moves more sideways. The influence of this inclination is noticeable at wind speeds over 10m/s and creates an error in the point clouds in the order of a few centimeters (Kuschnerus et al., 2021). These errors can be corrected by applying a transformation matrix, which is done in section 4.1.

Rain

Heavy rain (>4mm/hour) decreases the quality of the point clouds in two ways. First of all, wet paved ground does not return any signal (Kuschnerus et al., 2021), as the water hinders the return of the laser waves. Moreover, water drops drip from the roof of the hotel, directly in front of the laser instrument (Kuschnerus et al., 2021). These water drops scatter the waves and reduce the quality of the point cloud.

Water bodies
Water bodies absorb most of the laser radiation, instead of reflecting it. Therefore, the sea is not visible in the point clouds. In general, a surface with a higher moisture content reflects less (Anders et al., 2019).

Laser instrument
The settings of the laser instrument can also have a negative impact on the point clouds. For example, a power failure, a hardware failure, incorrect settings and differences in calibrations can occur.

2.4. Video data

In this section, the working principle of the video image processing is explained and limitations to the video data are given.

2.4.1. Working principle

Both the laser and the video data detect waves with a certain wavelength. However, in the case of video data, the instrument does not emit a pulse, but only detects incoming waves.

Video image processing uses arrays of pixels in two dimensions. Commonly, visual colours are displayed. However, many other types of images exist, for example, black-and-white images or images where infrared waves are displayed in a visual colour band (Holman et al., 1993). In this thesis, images of the true colours are used.

The most used video monitoring system in coastal research is the Argus system, which focuses on collecting images for research on hydrodynamics and bathymetry (Román-Rivera et al., 2020). A system based on the Argus system is the Horus system, which is used for this thesis.

2.4.2. Limitations

There are several limitations to the video data. These limitations are explained below.

Invisible areas
Not every area is visible in the video data. First of all, the view is limited by the camera. In addition, some areas in the video data are not visible, due to differences in elevation. For example, areas behind dunes and buildings can be invisible. Thirdly, when the intertidal area is below the water level, the marine processes can hardly be seen in the video data. The fourth reason for invisibility is darkness during nighttime. Only when an electric light or the moon illuminates (a part of) the image, information can be taken from the video data during nighttime.

Video instrument
In situ video monitoring systems might be a victim of vandalism if the instrument is placed at an accessible place. Furthermore, hurricanes and severe thunderstorms can damage the instrument. Maintenance is thus important to ensure continuous video data of the expected quality (Román-Rivera et al., 2020). The settings of the video instrument can also have a negative impact on the images. For example, an empty battery, moisture inside the camera or incorrect settings can occur.

Weather
As mentioned before, hurricanes and severe thunderstorms can damage the instrument. In addition, rain and clouds can also negatively impact the video data by reducing the image quality.

2.5. Related work

Coastal areas have been examined using video data before. By using video data, existing literature focuses on understanding natural deformations. Examples are topics like shoreline evolution (Smit et al., 2007), rip channels (Bogle et al., 2001), and coastal behaviour due to storms (Huguet et al., 2016). However, the role of anthropogenic interventions is often ignored in such research.

Terrestrial Laser Scanning is mainly used to examine natural deformation. Examples are researches on moisture content (Jin et al., 2021), sand moving towards dunes (Anders et al., 2019) and tidal bars (Vos et al., 2020). Anthropogenic deformation causes are not taken into account in many of these researches.

A few anthropogenic influences on beach areas are examined. First of all, the influence of anthropogenic structures is examined (Bosveld, 2020; McNamara and Werner, 2008; Rogers et al., 2015). Secondly, the visitor density is determined using video data (Aarninkhof and Cohen, 2006).

Still, the influence of heavy equipment on coastal areas is largely unknown. Although some images of bulldozers in storm events are noted, deformations caused by bulldozers are not characterized in laser data yet (Lazarus and Goldstein, 2019). This thesis closes this knowledge gap by developing a method to find deformations caused by bulldozers in laser data. Video data is used to verify anthropogenic causes.

3

Characteristics of the data

This chapter elaborates on the characteristics of the used laser and video data. First of all, a site description is given in section 3.1. Furthermore, information on the used laser and video intstruments is given in section 3.2 and 3.3. Finally, information on the available data is given in section 3.4.

3.1. Site Description

The area of study is located in Noordwijk, the Netherlands. The location of the site is visualised in Figure 3.1. West of Noordwijk lies the North Sea. The coastal area exists of a sandy beach strip. The width of the beach strip varies roughly between 50m at very high tide and 150m at very low tide. The beach strip is followed by a dune strip, being roughly 100 m wide. The dunes are 13 m above NAP at the highest level, with some low areas for passageways (AHN, 2022).

Figure 3.1: The position of Noordwijk in the Netherlands (Earth, 2022).

The laser instrument and camera were located on top of hotel Huis ter Duin. Figure 3.2a. shows an overview of the site, together with the visible areas in the laser and video data. The set-up is visible in Figure 3.2b.

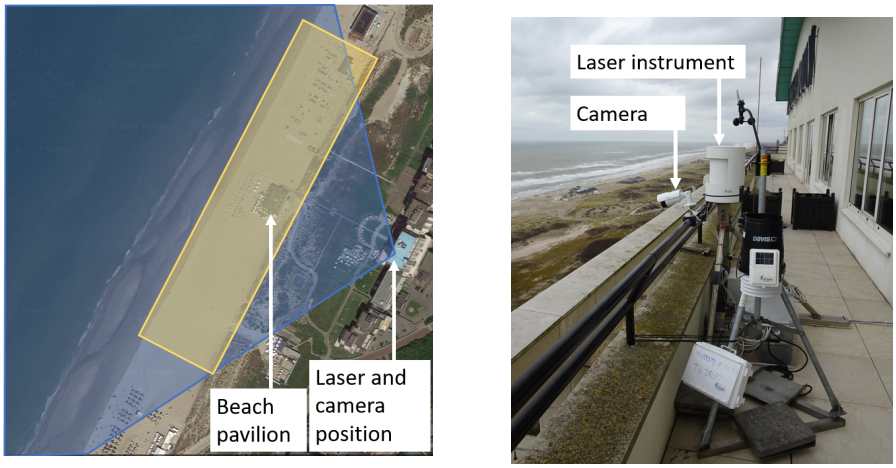

(a) Site overview of the beach at Noordwijk (Earth, 2022). The blue area is visible in the video data, the yellow area is the area used in the laser data.

(b) The camera and laser instrument on top of hotel Huis ter Duin.

Figure 3.2: The set-up of the laser and video instruments and their area of use.

3.2. Laser instrument

The laser scanner, as shown in Figure 3.2b, is a Riegl VZ-2000 instrument. The laser scanner is mounted on a frame and is protected against the weather by protective housing. The instrument has a vertical accuracy of 1-5 cm and a horizontal accuracy of 0.1-1 m. The instrument scans the beach at least every hour. The instrument is kept at the same position for years, so the coastal dynamics can be analysed on hourly to yearly temporal scales (Vos et al., 2017).

The instrument is safe for the human eye (Laser Class 1) and can therefore safely be used in the beach area, where humans are exposed to the laser. The instrument can view up to 100°x360° (Riegl, 2022). In the case of Noordwijk, the area of view is limited to the coastal area. An example of a point cloud generated by the laser data is visualised in Figure 3.3.

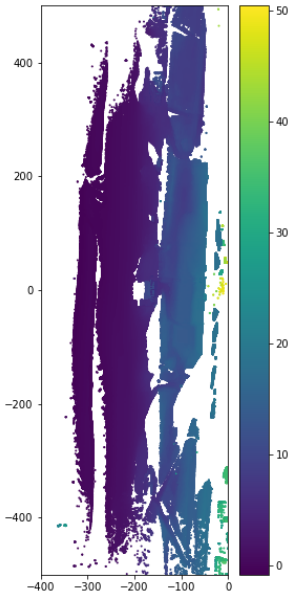

Figure 3.3: The area viewed with the laser instrument. The yellow area on the right indicates a high position. This high area is on top of the hotel, where the instrument is located. The dune area is at -150<x<-50, the beach area is the visible area at x<-150. The white area at x=-200, y=0 is a beach pavilion.

3.3. Video instrument

The position of the camera is shown in Figure 3.2b. The instrument was a 5-megapixel camera and was placed on the hotel in the period February 20 to April 26, 2020. The frequency of the video data changed multiple times during this time period, the details can be found in section 3.4. An example of the video data is visible in Figure 3.4.

Figure 3.4: An image taken from the video data. On the beach, the beach pavilion is visible. In the lower part of the image, a part of the balcony is visible.

3.4. Dates and data gaps

The video data is generated in the period from February 20, 2020, until April 26, 2020. That period is examined in this thesis. However, there are some gaps and peculiarities found in the available data.

Laser

The laser data is available for every half hour of all dates in the period February 20, 2020, until April 26, 2020. However, there are a few exceptions:

- There is no data available in the period from 5 April 14.00h until 14 April 11.15h. This gap of nine days is considerable in the observation period of sixty days.
- Between 23 February 20.30 and 24 February 23.00, only one point cloud is available, which is on 24 February 12.00.
- Aside from the point clouds on the hour and on the half hour, there are also point clouds available for the times 1.45, 6.45, 7.45, 12.15, 13.45 and 19.45.
- Point clouds of 12.30 do not exist.
- The point clouds of 23 March 20.30 and 29 March 2.00 and 2.30 are missing.

The availability of point clouds, however, does not say anything about the quality of the point clouds. Point clouds can, for example, be strongly reduced in area due to fog, as discussed in section 2.3.2. Some incomplete point clouds are present in the data. These point clouds are displayed in section 4.1.5.

Video

The video data changes in frequency multiple times during the observation period. On some days, the frequency was 5 Hz (five pictures per second). On other days, the frequency was lower with only one picture taken every five minutes (3.3 mHz). There is also a period where the frequency varies between 1 and 5 Hz. Note that a higher frequency means more pictures, and thus smaller time intervals, but also larger amounts of data. An overview of the days and the photo frequencies is given in Figure 3.5. In the overview, a data gap is visible from February 24 at 12:08 until February 25 at 14:20. Another data gap is visible from the afternoon of February 26 until February 28 at 21:00. A smaller data gap is present on February 26 from 10.45 until 11.00. Aside from these data gaps, a few data gaps of less than ten minutes are present. Those small gaps are assumed to be negligible in this research.

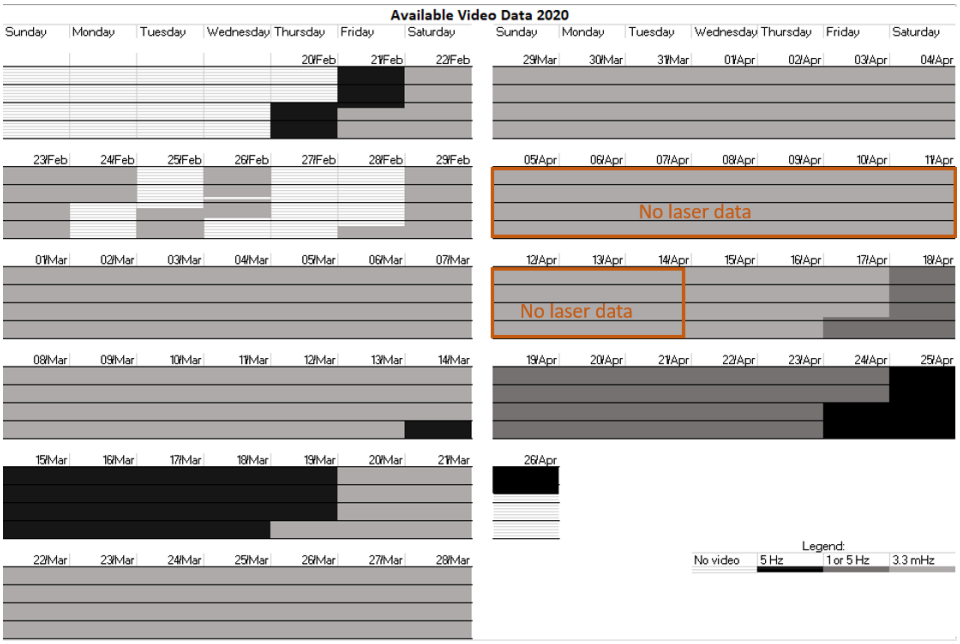

Figure 3.5: Overview of the available dates of the video and laser data.

4

Change detection analysis

In this chapter, the change detection method is given. Before using the laser data, the data is pre-processed, which is explained in section 4.1. Section 4.2 contains the change detection method to detect anthropogenic deformations in the laser data. The validation using video data is explained in section 4.3.

4.1. Pre-processing

The laser-generated point clouds are pre-processed before anthropogenic deformations are sought. First, data is selected. Then, transformations are applied, followed by clipping to the area of interest. Finally, the point cloud is reshaped to a grid and incomplete point clouds are checked. These steps are done using python programming. The code can be found in Appendix B.

4.1.1. Data selection

In this thesis, one point cloud of every day is taken. A time interval of a day is chosen, as anthropogenic deformations happen within several hours and will be visible as changes from one day to the next.

The point clouds are taken at varying moments of the day. The moment of the day depends on the tide. At high tide, the beach area is not fully visible. To prevent this, the point clouds of the hour close to low tide are taken. The moments of low tide in the period February 20, 2020, until April 26, 2020, are taken from Rijkswaterstaat tidal data in Scheveningen (Rijkswaterstaat, 2022).

4.1.2. Apply transformations

As explained in section 2.3.2, a transformation should be applied to correct for instrument movements caused by wind or other effects. In order to do this, two methods are possible. One works with an inclination sensor in the laser scanner. Roll and pitch transformation values are available for every point cloud. These values are used to transform the point clouds. The result of this transformation is visible in Figure 4.2.

Another way of correcting for movements of the laser scanner is to use reference points. Some surfaces, like a helicopter platform or a traffic sign, are clearly distinguishable and are not prone to natural changes. These points can be used as reference points. In this case, a small platform and the beach pavilion are used as reference points, see Figure 4.1. The position of these objects is compared to their position in a reference point cloud. A transformation from the original to the reference position of the reference points is made, which gives a transformation matrix for the whole point cloud. The transformation matrix belonging to a certain point cloud can then be used to transform the whole point cloud to the reference position. The result of this method is displayed in Figure 4.2.

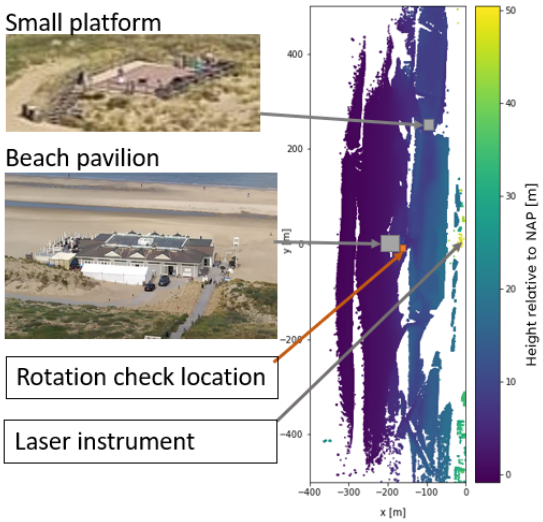

Figure 4.1: The location of the reference points 'small platform' and 'beach pavilion' used to create the transformation matrix. The location of the rotation check is also shown.

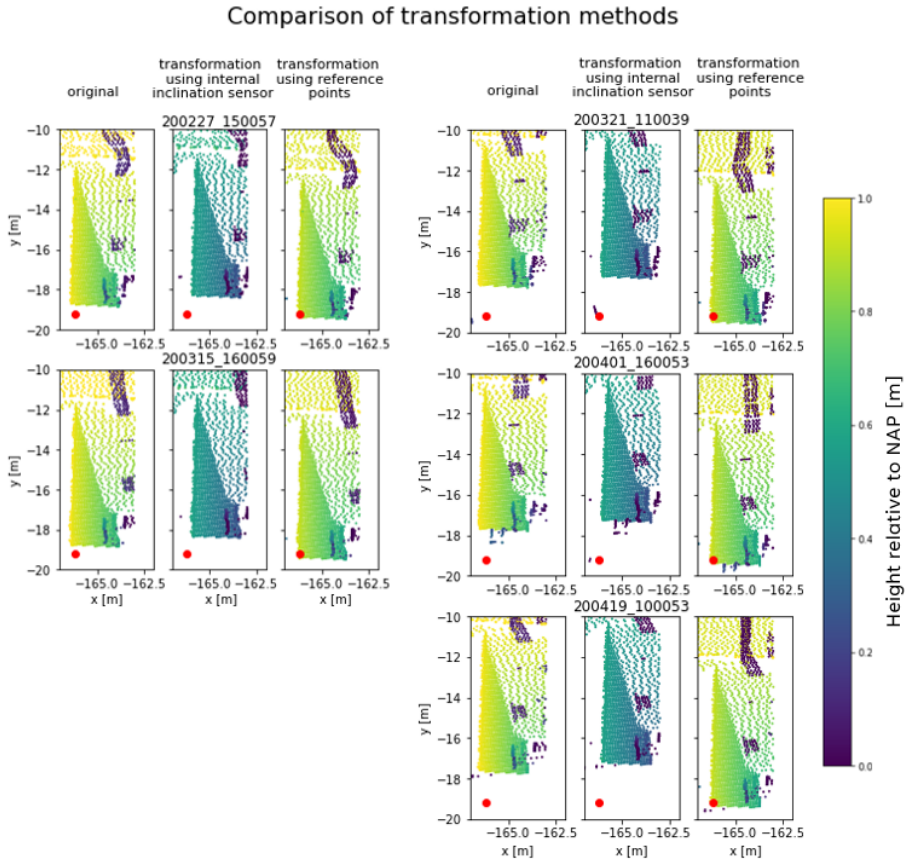

Figure 4.2: Transformation methods compared for different dates at a location close to the beach pavilion. The triangle shape is a ramp situated next to the beach pavilion. For every date, three images are given. The left image shows the original point cloud, the middle image shows the point cloud after transformation using the internal sensor. The right image shows the point cloud after transformation using reference points. The red dot is a set point to refer to.

From 4.2 it appears that the method using reference points is more accurate than the method using the internal laser sensor. Comparing the middle images (internal sensor correction) of the two dates on the left and the three dates on the right, the position of the dense triangle shape is clearly in a different position, varying around 1.5 m. In the right images (reference point correction), the position of the triangle is more constant. There, the deviation is in the order of 10 cm. As the matrix file gives a more accurate transformation, this method is used in the rest of the thesis.

Other coördinate systems and NAP
Aside from the transformation due to movement of the laser instrument, transformations to other coördinate systems are also possible. However, a transformation to a general coördinate system, such as the Dutch RD-system, is not needed for this thesis. The local coördinate system is thus used. The local coördinate system is based on the position of the laser. In the original point clouds, the point (0, 0, 0) is the position of the laser instrument.

An additional transformation is applying a height correction, which is done in this thesis. NAP is an important Dutch reference height and is used in this thesis as a reference height. The instrument on the hotel is located at 56.755 m above NAP. To correct for this height difference, 56.755 m is subtracted from every z-value of the point clouds.

4.1.3. Clip to the area of interest

The point clouds contain outliers which should be removed. Moreover, not the whole scanned area is of interest, but only the beach area is analysed in this research. Therefore, boundary values in x-, y- and z-direction are determined. An overview of these values in the local reference system is given in Table 4.1. Note that the local reference system is based on the location of the laser instrument. Therefore, the coördinates of the laser instrument are (0, 0, 56.755). The z-value is non-zero due to the correction of the height difference to NAP level.

Table 4.1: x-, y- and z-values of the boundaries of the area of study

Direction	Min	Max	Remark
x	-250	-150	Values of -150 to -50 contain the dune area, and are filtered out here
y	-250	250	Selects a 500 m long part of the beach near to the hotel
z	0	12	

4.1.4. Gridding

To decrease the running time for calculations, the number of points can be reduced. In this thesis, this reduction is done by using a grid. A grid of cells with size 1x1m is made. With the boundaries given in Table 4.1, this amounts to 50,000 grid cells. Roughly 40,000 cells have values, other cells lack points as the area is invisible to the laser instrument.

Ultimately, by using boundaries and using a grid, the number of points reduces from around 9,000,000 points to around 40,000 points.

4.1.5. Check on incomplete point clouds

Some point clouds are incomplete. In Figure 4.1.5, some remarkable point clouds are visualised.

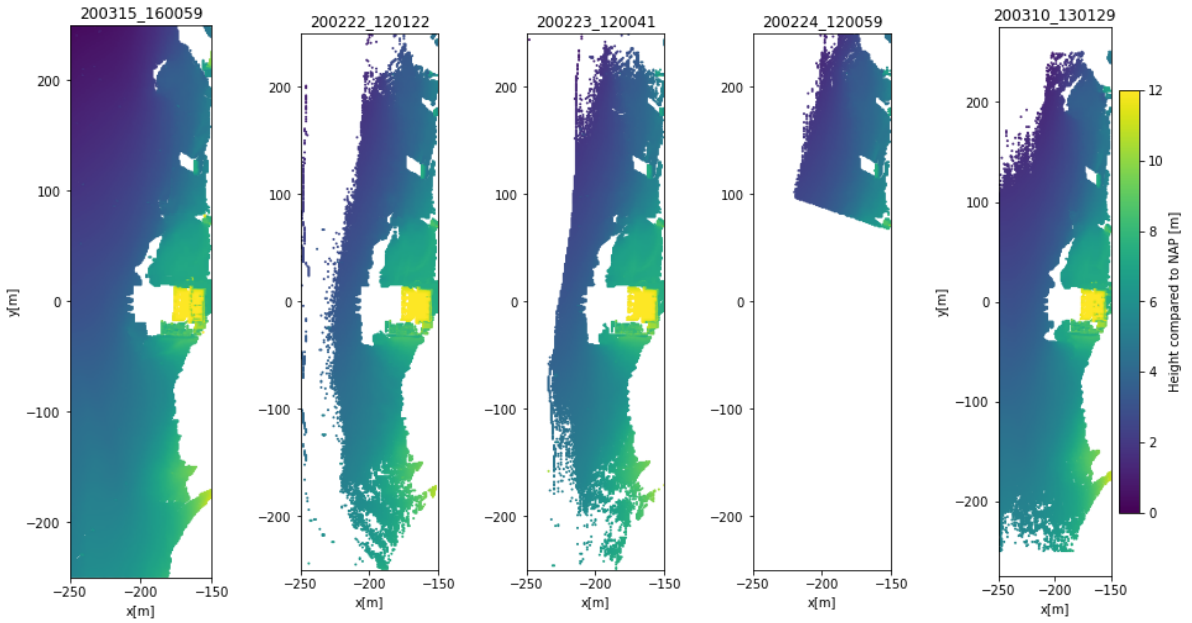

(a) On March 15, 2020 16:00, a complete point cloud is visible.

(b) On February 22, 2020 12:00, part of the intertidal area is missing.

(c) On February 23, 2020 12:00, part of the intertidal area is missing.

(d) On February 24, 12:00, a large part of the point cloud is missing.

(e) On March 10, 2020 13:00, the left corner areas are missing.

Figure 4.3: A complete and four incomplete point clouds.

The following causes explain the incomplete point clouds:

- The only available point cloud of February 24 misses more than half of the area. For the rest of that day, there were no point clouds available. Thus, there has been a problem with the laser instrument on February 24. The data of this date is therefore not useful in this research and February 24 is skipped in the laser data.
- On some days, points are missing in the left corner areas, see Figure 4.3e. The missing corner areas are caused by the influence of rain and mist. The point cloud where this influence is most visible is the point cloud of March 10, 2020. Figure 4.4 shows there was rain indeed on that day.

Figure 4.4: The image quality on March 10, 2020 is reduced by rain. This rain disturbed the point cloud of that day.

- Incompleteness of the point clouds on February 22 and 23 could have been caused by high water levels at low tides. Nonetheless, tidal data shows that the low tide water level should be even

higher on February 21 (Rijkswaterstaat, 2022). On that day, however, the area close to the sea is not missing in the point clouds. Another cause for the disturbances is therefore sought. A reasonable explanation is that the laser instrument was not functioning well on these two days, as the day after, on February 24, data is missing due to an error in the laser instrument.

4.2. Change detection in laser data

After the pre-processing, where data is selected, transformations are applied, the area of interest is clipped and gridded and incomplete point clouds are checked, the change detection is carried out.

The change detection in the laser data consists of two steps. First, a visual analysis is carried out to link deformation causes to deformations in the laser data. Secondly, a decision tree is made to filter out non-anthropogenic deformations.

4.2.1. Visual analysis

The height difference between two consecutive days is visualised for every time interval. An example of the time interval from March 28 to 29 is shown in Figure 4.5. These visualisations are then visually examined to find characteristics that match the deformation causes described in chapter 2. The results of the visual analysis can be found in section 5.1.

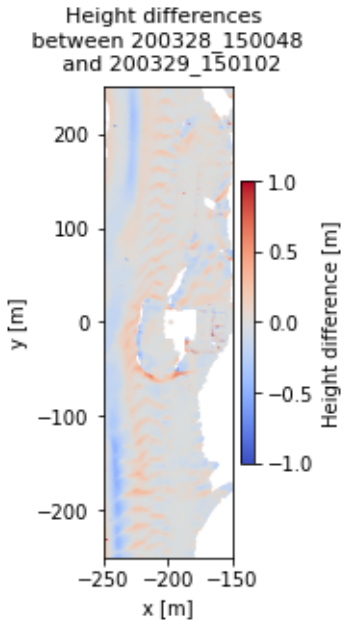

Figure 4.5: The height difference between the point clouds of March 28 and 29. Images like this are made for every time interval and visually analysed to detect characteristics of deformations.

4.2.2. Decision tree

Based on the results of the visual analysis of the height difference maps, see section 5.1, a decision tree is made to filter out deformations with characteristics of other causes. The decision tree is displayed in Figure 4.6.

The decision tree is used for every image of height differences between two days. Deformations which do not match the criteria of sand waves, tidal bars, vehicles and small-scale deformations are labelled as anthropogenic. These anthropogenic labelled deformations are later validated in the video data.

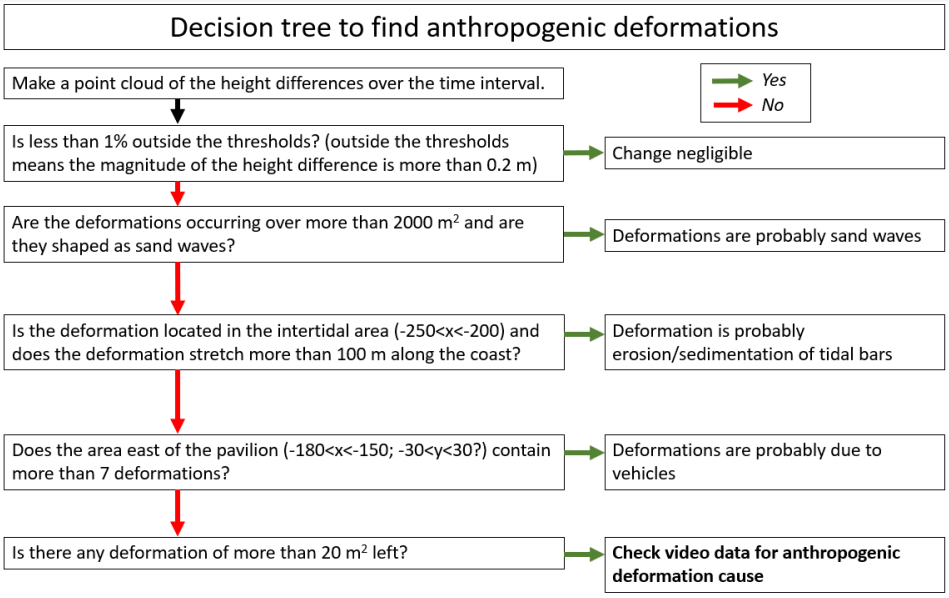

Figure 4.6: The decision tree used to check possible causes of deformations. When the characteristics of sand waves, tidal bars and vehicles do not apply for a deformation, the deformation is checked in the video data.

The criteria to filter out sand waves, intertidal bars, vehicles and small deformations follow logically from the results of the visual analysis:

- Erosion and sedimentation are visible in the intertidal area (-250<x<-200). These deformations stretch at least 100m along the coast in the cases of the visual analysis. Thus, the intertidal area and the length of the deformation in y-direction are taken as characteristics to filter out sedimentation and erosion in the intertidal area.
- Sand waves can be recognized using the typical wave-like shapes and the large area (>2000 m^2, e.g. 40x50m) over which they occur.
- In the area east of the beach pavilion (-180<x<-150; -30<y<30), vehicles are often present. If this area contains many small deformations, vehicles are expected to be the deformation cause and this area is filtered out.
- Small-scale deformations are filtered out using two criteria. The first criterion filters out images where less than 1% of the area changed more than 0.2m in height. This filters out images with little deformations and deformations of insignificant height compared to the expected height differences caused by heavy equipment. The second criterion filters out deformations of less than 20 m^2. This filters out deformations due to human presence and temporarily placed objects. The choice for these values is determined by a trial-and-error process, whilst examining the point clouds.
- Dune growth and the influence of buildings were not found in the visual analysis. Thus, these deformation causes are not part of the decision tree.

Note that all given values are specific for the location in Noordwijk, using the local coördinate system. The values might also differ in other time periods. Different values should be taken when the decision tree is applied to another area, time or coördinate system.

4.3. Validation in video data

The decision tree leads to expected anthropogenic deformations. Validation of the anthropogenic causes is done using video data. For every expected anthropogenic deformation, the time interval and coördinates are taken from the table in section 5.2. The video data of that time interval is watched, focusing in particular on the area of the deformation. When the anthropogenic cause, often being a

bulldozer, is visible in the area of deformation, an image is taken from the video. Bulldozers must be seen in at least two images (images are made every 5 minutes on most days) to filter out bulldozers that only pass by.

In some other cases, other images are also taken from the video. First and foremost, when there is no anthropogenic cause visible, but there are signs of another deformation cause in the video, an image is taken to explain other deformation causes. Secondly, the presence of sand waves is validated in three cases. Sand waves are visible on the video data as darker and lighter sand, for the tops of sand waves have a lower moisture content and are therefore lighter. This is explained in section 2.1. Thirdly, some images of vehicles are taken to show the frequent presence of vehicles east of the beach pavilion. Fourthly, some additional images are taken to show other important findings, such as low image quality.

5

Results

This chapter contains the results of the change detection analysis. In section 5.2, the results of the decision tree are shown. In section 5.3, the results of the validation in the video data are shown. This section shows images of the video data with anthropogenic causes, possible other causes and other remarkable findings.

5.1. Visual analysis of laser data

Deformation causes described in chapter 2 were found in the visualisations in the following manner:

- Erosion and sedimentation due to marine processes are visible in the intertidal area. The intertidal area in Noordwijk is located in the area -250<x<-200, using the local coördinate system. The erosion and sedimentation stretch along the coast, with more than 100m. In Figure 5.1, erosion is visible in the areas A.

- Typical wave-like shapes are found in a few time intervals and are expected to be sand waves. In Figure 5.1, sand waves are visible in the areas B. If sand waves occur, they often occur over a large area (>2000 m^2) of the beach.

- Dune growth is not found in the visual analysis, as the dune toe area was invisible in the laser data.

- The area around the beach pavilion was examined to find any deformation caused by buildings. No such cases were found.

- Small-scale deformations were found in many cases. These deformations are in the order of a few m^2 and can for example be caused by the temporary presence of humans, vehicles or placement of waste bins on the beach. Another way to characterize small-scale deformations is to look at the height difference. From the images follows that deformations with a height difference up to roughly 0.2m can be classified as low deformations.

- In the area east of the beach pavilion (-180<x<-150 and -30<y<30), many small deformations (<10 m^2) are visible. An exploratory examination of the video data showed vehicles were often parked in this area. In Figure 5.1, small deformations due to vehicles are visible in the area C.

- Deformations caused by heavy equipment could not be characterized yet. However, some deformations did not have characteristics of other deformations causes and may be caused by heavy equipment.

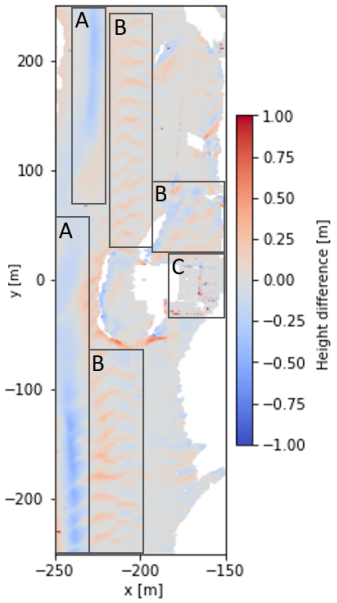

Figure 5.1: The height difference between the point clouds of March 28 and 29. Characteristics of erosion in the intertidal area (A), sand waves (B) and vehicles (C) are visible in this time interval.

5.2. Apply decision tree to laser data

The decision tree is displayed and explained in section 4.2.2. The results of the decision tree are displayed in Table 5.1.

In total, 57 time intervals in the period February 20, 2020, until April 26, 2020, are used. 23 time intervals had more than 1% of the area outside the thresholds of -0.2 and +0.2m. Only those 23 point clouds are used to determine causes of deformations. Of these 23 point clouds, 4 had deformations matching the sand waves criterion. 11 point clouds had deformations matching the erosion/sedimentation criterion. All 23 point clouds contained deformations matching the vehicle criterion. 20 point clouds had deformations left of more than 20[m^2] and are taken to the next step: validation of the anthropogenic cause in the video data.

Table 5.1: Outcomes of the decision tree

From (MMDD_ HHMMSS)	To	>1% outside thresholds	Sand waves	Erosion/ sedimentation intertidal area	Vehicles	Deformations >20[m^2] left?
0220_100047	0221_110109	1.43%	no	no	yes	yes
0221_110109	0222_120122	3.51%	yes	no	yes	yes
0222_120122	0223_120041	1.74%	yes	no	yes	yes
0223_120041	0225_130123	2.91%	no	no	yes	yes
0225_130123	0226_140138	no				
0226_140138	0227_150057	1.15%	no	no	yes	yes
0227_150057	0228_150114	1.12%	no	no	yes	yes
0228_150114	0229_160131	no				
0229_160131	0301_160050	1.11%	no	yes	yes	yes
0301_160050	0302_150110	1.20%	no	no	yes	
0302_150110	0303_160126	no				
0303_160126	0304_190046	no				
0304_190046	0305_200104	no				
0305_200104	0306_220124	2.68%	no	no	yes	yes
0306_220124	0307_230042	no				
0307_230042	0308_110051	no				
0308_110051	0309_120110	no				
0309_120110	0310_130129	1.03%	no	no	yes	yes
0310_130129	0311_140046	2.85%	no	yes	yes	yes
0311_140046	0312_140103	2.42%	no	yes	yes	yes
0312_140103	0313_150123	1.92%	no	yes	yes	yes
0313_150123	0314_160041	no				
0314_160041	0315_160059	no				
0315_160059	0316_170117	1.48%	no	yes	yes	yes
0316_170117	0317_180037	no				
0317_180037	0318_180052	1.79%	no	yes	yes	yes
0318_180052	0319_190111	no				
0319_190111	0320_210030	no				
0320_210030	0321_110039	no				
0321_110039	0322_120057	no				
0322_120057	0323_120116	1.45%	no	no	yes	yes
0323_120116	0324_130035	1.60%	no	no	yes	yes
0324_130035	0325_130052	1.97%	no	yes	yes	yes
0325_130052	0326_140110	2.08%	no	yes	yes	no
0326_140110	0327_140027	no				
0327_140027	0328_150048	no				
0328_150048	0329_150102	7.24%	yes	yes	yes	yes
0329_150102	0330_160019	no				
0330_160019	0331_160037	no				
0331_160037	0401_160053	1.29%	no	no	yes	yes
0401_160053	0402_180012	no				
0402_180012	0403_200034	1.17%	yes	yes	yes	no
0403_200034	0404_210052	no				
0404_210052	0405_110100	no				
Missing data						
0413_160113	0414_040026	no				
0414_040026	0415_050039	yes, 4.19%	no	yes	yes	yes
0415_050039	0416_050057	no				
0416_050057	0417_060019	no				
0417_060019	0418_080035	no				
0418_080035	0419_100053	no				
0419_100053	0420_110012	no				
0420_110012	0421_120028	no				
0421_120028	0422_120046	no				
0422_120046	0423_120003	no				
0423_120003	0424_130024	no				
0424_130024	0425_130038	no				
0425_130038	0426_135955	no				

5.3. Validation of anthropogenic causes in video data

Possible anthropogenic causes for deformations are validated in the video data. The results of this validation are summarized in Table 5.2. A total of 30 deformations are marked as possibly anthropogenic caused. 16 of these deformations are linked to the presence of bulldozers. Of the other 14 cases, 6 cases are linked to sedimentation or erosion against a building or container, 4 cases could not be validated due to a gap in the video data, 2 locations were invisible (one behind the dunes, one out of the visible area), 1 cause might be tidal sedimentation/erosion or an unclear anthropogenic cause, and 1 case is caused by a vehicle placed on the beach.

All images resulting from the validation in the video data can be found in A. In this section, the images are mainly used to exemplify.

Table 5.2: Outcomes of the video validation. In total, 30 deformations were marked as possibly anthropogenic caused in the point clouds.

From (MMDD_ HHMMSS)	To	x-coördinate	y-coördinate	Bulldozer visible at deformation location	Remark
0220_100047	0221_110109	-220	-50	yes	
		-180	-150	no	Invisible, behind dunes
0221_110109	0222_120122	-170	-30	no	Sedimentation against building?
		-160	120	no	Erosion against container?
0222_120122	0223_120041	-170	-30	no	Sedimentation against building?
		-160	120	no	Sedimentation against building?
0223_120041	0225_130123	-160	-30	yes	
		-200	-80	yes	
0226_140138	0227_150057	-160	180	no	No video data available
		-180	-180	no	No video data available
0227_150057	0228_150114	-180	30	no	No video data available, yet tire tracks seen at this location the next morning.
		-170	90 to 140	no	No video data available
0229_160131	0301_160050	-180	-30	no	Sedimentation against container or work at night?
0301_160050	0302_150110	-180	-30	yes	
0305_200104	0306_220124	-180	200	no	Invisible, out of visible area
0309_120110	0310_130129	-180	-30	no	Sedimentation against container?
0310_130129	0311_140046	-200	-30	yes	
0311_140046	0312_140103	-180	-180	yes	
		-220	-30	yes	
0312_140103	0313_150123	-220	-20	yes	Same bulldozer as deformation above
0315_160059	0316_170117	-220	-10	yes	
0317_180037	0318_180052	-180	-40	yes	
		-220	-30	yes	
0322_120057	0323_120116	-220	from -50 to 50	yes	Two bulldozers
0323_120116	0324_130035	-220	from -50 to 50	yes	Lot of heavy equipment present and working the whole afternoon.
0324_130035	0325_130052	-210	50	no	A vehicle was temporarily placed on the beach
0328_150048	0329_150102	-220	from -30 to 20	no	Erosion/sedimentation by tide or unclear human influence
0331_160037	0401_160053	-220	from -20 to 20	yes	
0414_040026	0415_050039	-220	from -50 to 30	yes	
		-180	-30	yes	Two bulldozers

5.3.1. Expected anthropogenic cause found

In sixteen cases, a bulldozer was found at the location of the deformation. The deformations caused by heavy equipment are found to displace more than $50m^2$ in all cases. An example of a bulldozer causing a deformation, together with an image of the laser data is given in Figure 5.2. Similar images of the other cases can be found in appendix section A.1.

In total, there are 15 anthropogenic interventions, as one bulldozer influenced two point clouds at the same location around the transition moment of two time intervals on March 12, 2020. Remarkable results appeared on March 23, 2020, where a lot of heavy equipment was present and working in the area of deformation. In two other cases, two bulldozers were present and working, being in the morning of March 23 and the morning of April 14.

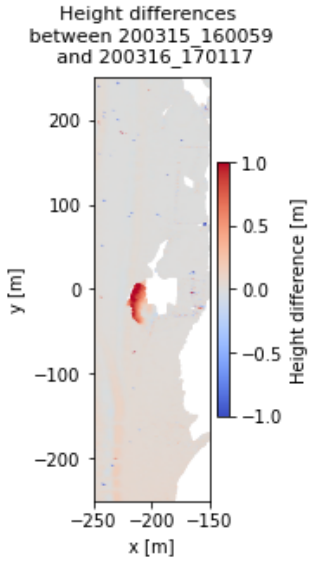

(a) Histogram and point cloud.

(b) A bulldozer is present in the area of deformation.

Figure 5.2: Bulldozer on the morning of March 16, 2020 around x=-220 and y=-10.

5.3.2. Expected anthropogenic cause not found

In fourteen deformation cases, bulldozers were expected but not found in the video data. In this section, results pointing towards other causes are given.

Influence of buildings and containers

In six cases, erosion or sedimentation against freight containers is expected to be the deformation cause. Figure 5.3 shows the locations of these deformations, together with images of the containers at those locations. Erosion and sedimentation against containers occurs at two locations: around x=-170 y=-30 and x=-160 y=-120, both close to the containers. In addition, in some of these time intervals, flags are present in front of the hotel, indicating a strong wind, see Figure 5.4. From the location and the indication of strong wind follows the conclusion: Aeolian sand transport is expected to be the cause for the sedimentation/erosion next to the freight containers.

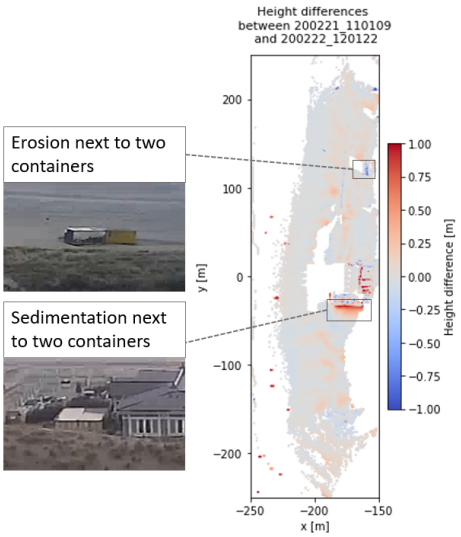

Figure 5.3: Erosion and sedimentation in the time period February 21 to 22. The expected anthropogenic deformations around x=-170 y=-30 and x=-160 y=-120 are close to freight containers placed on the beach. Erosion and sedimentation due to wind might explain these deformations.

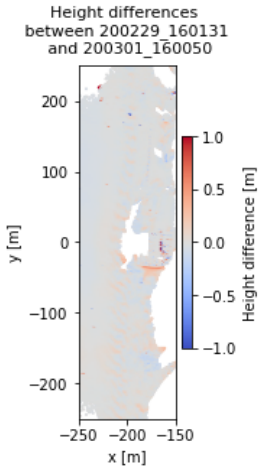

(a) Point cloud of the height differences over a time interval.

(b) Flags indicate a strong wind from the south, possibly causing sedimentation against the container.

Figure 5.4: No bulldozers are seen between February 28 and February 29 around x=-180 y=-30 (location of container). The flags indicate a strong wind. Aeolian sand transport is expected to be the cause for the height increase next to the freight container.

Gap in video data

Between the afternoon of February 26 and February 28 at 21:00, no video data was available. Four deformations could not be checked for this reason. However, on the morning of February 29, tire tracks are visible around x=-180 y=-30. A deformation around that location is also found in the point cloud of February 27 to 28. So, there is strong evidence that the deformation between February 27 and 28 around x=-180 y=-30 has an anthropogenic cause. See Figure 5.5 for the images.

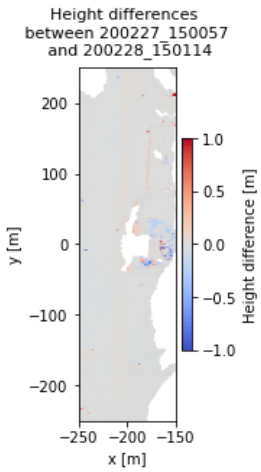

(a) Point cloud of the height differences over a time interval. Video data of this period is unavailable.

(b) tire tracks are visible on the morning of February 29, 2020.

Figure 5.5: No video data is available in the period February 27 to 28, but tire tracks are visible in the morning of February 29, 2020 around x=-180 y=30.

Invisible areas

Two locations were not visible in the video data. In Figure 5.6, the area of deformation is located behind a dune. In Figure 5.7, the area of deformation is located right of the video frame and is therefore not visible.

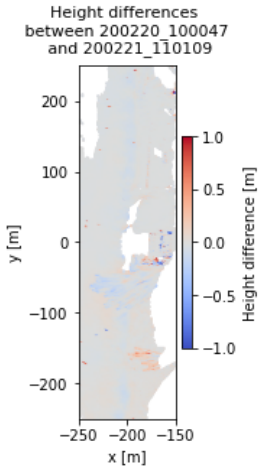

(a) Point cloud of the height differences over a time interval.

(b) Area of deformation around x=-180 y=-150 is not visible due to dunes.

Figure 5.6: In the period February 20 to 21, the deformation around x=-180 y=-150 is not visible due to dunes.

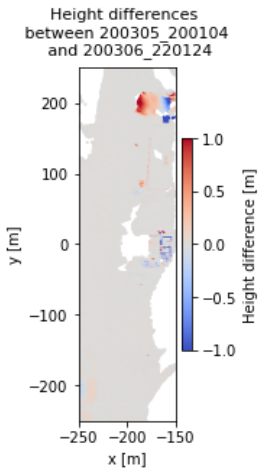

(a) Point cloud of the height differences over a time interval.

(b) A bulldozer is seen. However, the area of deformation (x=-180, y=200) is more to the right, and is not visible in the video data.

Figure 5.7: In the period March 5 to 6, 2020, the deformation of x=-180, y=200 lies outside the visible area of the video data.

Vehicle on the beach

In one case, a vehicle was placed on the beach, see Figure 5.8. This vehicle deformed around 20 [m^2].

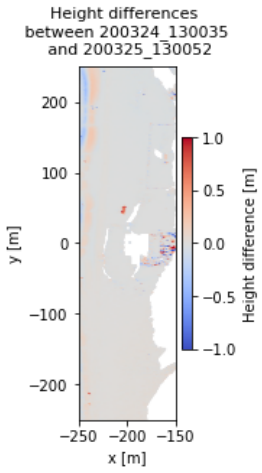

(a) Point cloud of the height differences over a time interval.

(b) A vehicle is placed on the beach, at the location of the deformation.

Figure 5.8: In the period March 24 to 25, 2020, a vehicle is placed on the beach, causing a deformation at x=-210, y=50.

Tidal erosion/sedimentation or unclear anthropogenic cause
In the time period March 28 to 29, the quality of the video data is low. There could be an anthropogenic cause of the deformation around x=-220 and -20<y<20, see Figure 5.9c and 5.9d. However, the tide may also be the cause of the deformation, see Figure 5.9b.

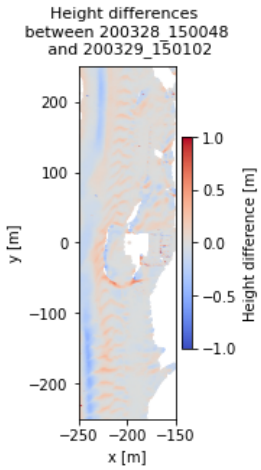

(a) Point cloud of the height differences over a time interval.

(b) High tide in the period March 28 to 29. The deformation in the area x=-220 and -20<y<20 might be caused by erosion and sedimentation.

(c) Before possible human intervention.

(d) Possibly, human intervention is visible in this image at the location of deformation.

Figure 5.9: In the period March 28 to 29, 2020, the quality of the video data is low. Still, anthropogenic influence might be visible around x=-220,-20<y<20. Another cause for this deformation can be erosion and sedimentation.

5.4. Additional results video data

In the video data, not only the anthropogenic deformations are validated. Also, the assumptions of the decision tree are checked as far as possible. Furthermore, low image quality images are shown and some other remarkable results are shown as well.

5.4.1. Unexpected anthropogenic deformations

In the point clouds filtered out with the 1% criterion, a remarkable deformation was found in the time interval March 19 to 20. This deformation is validated in the video data, see Figure 5.10 and was indeed an anthropogenic deformation. The implications hereof are further discussed in the discussion, section 6.1.

Another working bulldozer was found by accident in the video data of April 3, 2020, see Figure 5.11. The bulldozer seems to have been replacing waste bins.

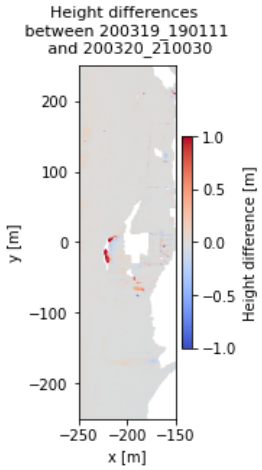

(a) Point cloud of the height differences over a time interval.

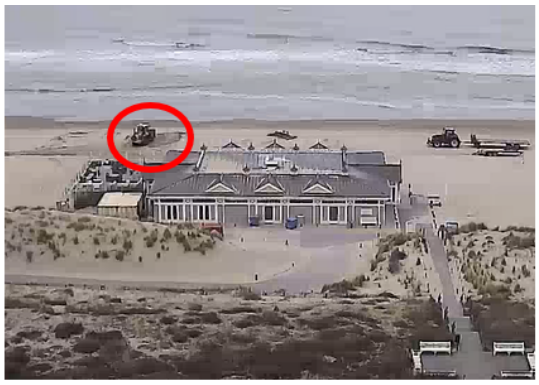

(b) A bulldozer is working and causing a deformation around x=-220 and y=0.

Figure 5.10: A bulldozer is working and causing a deformation in the time interval March 19 to 20. The point cloud was filtered out as less than 1% of the area had deformations outside the thresholds of -0.2 and +0.2 [m].

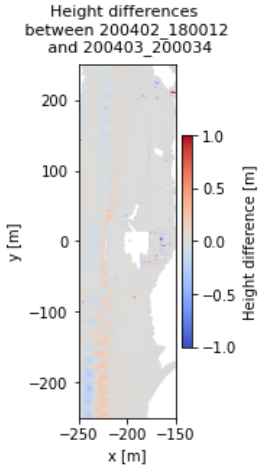

(a) Point cloud of the height differences over a time interval.

(b) A bulldozer is visible and seems to replace waste bins.

Figure 5.11: A bulldozer seems to replace waste bins on the morning of April 3, 2020. The resulting deformation in the point cloud is negligible (<20[m^2]).

5.4.2. Vehicles and sand waves check

The vehicle criterion in the decision tree follows from the fact that many vehicles were seen east of the pavilion in the video data. Exemplary images of those vehicles can be found in Figure 5.12, yet many

more cases could have been taken to illustrate.

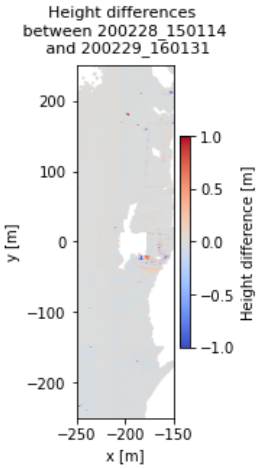

(a) Many point clouds show small deformations east of the beach pavilion (in the area -180<x<-150 and -30<y<30). This time interval is used to exemplify.

(b) Bus in front of restaurant on February 21, 2020.

(c) A loading truck in front of restaurant on March 6, 2020.

(d) Car in front of restaurant on March 9, 2020.

Figure 5.12: The area -180<x<-150 and -30<y<30 contains many small deformations. Cars, buses and trucks are often the cause of these small deformations.

The criterion of sand waves is checked in three cases. In all three cases, sand waves were visible in the video data. An example is given in Figure 5.4.2. All three cases can be found in appendix section A.4.

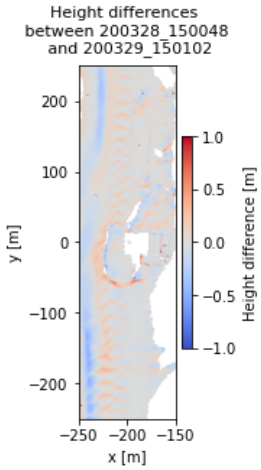

(a) Point cloud of the height differences over a time interval.

(b) Sand waves visible on March 29, 2020.

Figure 5.13: Validation check in video data of sand waves.

5.4.3. Image quality

The quality of the images is dependent on the weather. This is shown in Figure 5.14.

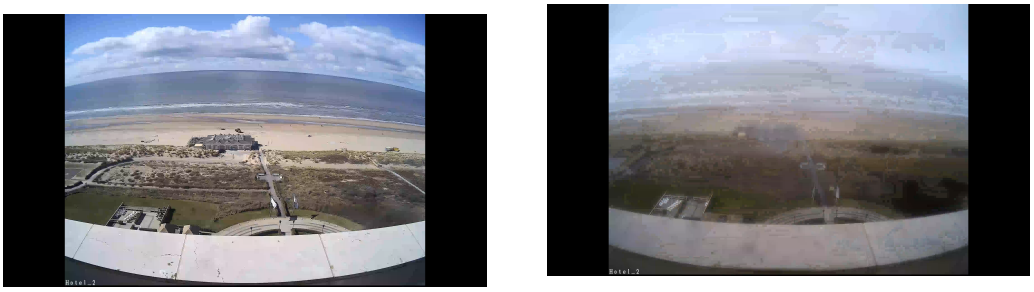

(a) High image quality on April 1, 2020.

(b) Very low image quality in case of rain. The image is taken from the video data of March 30, 2020.

Figure 5.14: The image quality is dependant on the weather. The image quality is lower on clouded, rainy days.

6

Discussion

In this chapter, the results are discussed. In section 6.1 the criteria used in the decision tree are discussed. Section 6.2 explains alternative deformation causes for the cases where anthropogenic influence was expected, but not found in the video data. These two sections lead to section 6.3, where improvements of the decision tree are given. The limitations of the laser and video data are discussed in sections 6.4 and 6.5.

6.1. Criteria of the decision tree

The used decision tree has some limitations and can be improved.

The first point to mention is that the used values are based on the data of Noordwijk, using the local coördinate system, in the time period February 20 to April 26, 2020. In other areas, coördinate systems and time periods, the used values may not apply and values must be replaced by values that are specific for that case. For example, the intertidal area is between the x-values of -250 and -200 in this case, but in Kijkduin, in the RD-coördinate system other values for the intertidal area are needed. Also, due to sea level rise, the intertidal area can shift more towards the dunes over time, impacting the values that determine the intertidal area.

Small-scale deformations I

In the decision tree, the criterion '*Is less than 1% outside the thresholds?*' is used. Outside the thresholds means the magnitude of the height difference is more than 0.2 m. The 0.2m value is based on visual analysis of the height difference images and filters out deformations with little height difference. Optimalisation of this value can be done, as values of 0.1 to 0.3m may give more accurate results.

The 1% is chosen based on visual inspection. Although this rule filtered out point clouds with very little deformations, there is a case found to be filtered out unjustly. On April 3, 2020, a bulldozer is linked to a deformation in a point cloud with less than 1% outside the thresholds of -0.2 to 0.2 m. Preventing such cases could be done in two ways: by lowering the percentage or by removing this criterion from the decision tree. Lowering the percentage can be done. However, the 1% criterion adds little to the decision tree when all other criteria, which have a better underpinning in literature, are applied. Thus, this criterion is unnecessary at last.

Sand waves

The criterion of the sand waves '*Are the deformations occurring over more than 2000 m^2 and are they shaped as sand waves?*' functions well. Three cases of sand waves, as found in the point cloud according to the criterion, are validated in the video data. In all three cases, sand waves were visible. Furthermore, deformations that were labeled as 'not caused by sand waves' were never found to be sand waves.

Tidal bars

The criterion of the intertidal bars '*Is the deformation located in the intertidal area (-250<x<-200) and does the deformation stretch more than 100 m along the coast?*' also functions well. No deformation marked as intertidal bar appeared to have an anthropogenic cause in the validation video data.

Vehicles
The vehicle criterion *'Does the area east of the pavilion (-180<x<-150; -30<y<30?) contain many small deformations?'* follows from the visual analysis. Every time interval had many small deformations in this area and thus, this area is always filtered out. Hereby, deformations caused by heavy equipment in this area may be missed. An improvement would be to filter out only deformations of more than 1.0m height difference in this area, as vehicles are mostly higher than 1.0m, but deformations caused by heavy equipment is often lower than 1.0m.

Small-scale deformations II
The criterion '*Is there any deformation of more than 20 m^2 left?*' follows from a trial-and-error process in the visual analysis. Small deformations, which may be caused by the temporary presence of humans and objects, are filtered out in this way. The value of 20m^2 is an estimation of small-scale deformations, found in the visual analysis. The deformations caused by heavy equipment are found to displace more than 50m^2 in all cases, and thus the value of 20m^2 can be replaced by a value between 40 and 60m^2.

6.2. Other deformation causes

Of fourteen deformations marked as anthropogenic caused, no anthropogenic cause could be found in the video data. This follows from the results section 5.3. Multiple other causes for those deformations are found.

First and foremost, aeolian sand transport is influenced by buildings and freight containers, which is expected cause in six cases. These deformations occurred at two specific locations (x=-170 y=-30 and x=-160 y=120) next to freight containers.

Four deformations could not be checked in the video data, as there was a gap in the video data between February 26 and February 28. For one of these deformations, however, tire tracks are seen at the location of deformation on the morning of February 29. Thus, this deformation is therefore likely to be caused by an anthropogenic cause.

Two deformation causes could not be checked, as the area of deformation was invisible. One deformation was behind the dunes, where anthropogenic causes cannot be seen. Another deformation was out of view.

In the remaining two cases, one deformation was formed by a vehicle on the beach and one deformation has an unclear cause. The quality of the video data was low on that day. Still, two possible causes are found: tidal erosion/sedimentation or an unclear anthropogenic cause could be the reason for this deformation.

6.3. Improvements to the decision tree

The criteria for the sand waves and erosion and sedimentation in the intertidal area functioned well. A criterion filtering out time intervals with little deformations did not help to find anthropogenic deformations, as at least one anthropogenic case was unjustly filtered out. Thus, it is better to leave out this criterion from the decision tree.

The sand wave and tidal bar criteria functioned well and further improvements of these criteria is not needed.

The vehicle criterion applied in all cases. This criterion can be made more specific, by using the height of vehicles (>1.0m).

The criterion filtering out small deformations areas can have a higher value (from 20m^2 to 40-60m^2), as all deformations caused by heavy equipment were larger than 50m^2.

An additional criterion can be added to filter out deformations due to freight containers. Deformations in the areas x=-170; y=-30 and x=-160; y=120 along the side of the freight containers can be labelled as 'caused by erosion/sedimentation due to freight containers'.

6.4. Limitations of the laser data

Usage of the laser data is limited by several factors. The causes of and impacts on the results are explained below.

Gaps in the data

A few causes lead to gaps in the data. First of all, some dates do not have any point clouds, probably due to an error in the laser instrument. From April 5 until April 13, 2020, the laser data is missing. This reduces the period of examination by around 10%. The point cloud of February 24 is incomplete, as less than a third of the usual area is visible. The cause is found to be an error in the laser instrument. As this was the only point cloud available for that day, the point clouds of February 23 and February 25 are used to determine deformations between two days.

Missing areas

The point clouds of February 22 and 23 are incomplete, probably by an error in the laser instrument, but still contain more than half of the usual area. These point clouds are still used in the change detection analysis, but some deformations close to the sea might therefore be missed in the time interval February 22 to February 25.

The left corners of the point clouds may contain fewer points, due to fog or rain. The clearest case in the examined time period is found on March 10, 2020. In that case, an area of roughly 100x50m is missing in the point cloud due to the weather. This effect due to rain and fog may lead to unseen deformations from March 9 until March 11.

Some areas are not visible, as they are behind a higher object. In the applied case, these higher objects causing 'laser shadow' are mainly the dunes and the beach pavilion. Deformations at the dune toes and on the seaside of the beach pavilion may thus be unseen due to the 'laser shadow' effect.

Alignment

The alignment of the laser data was tested with two methods. The first method, using wind information from the laser instrument, had deviations in the order of 1.5m. The second method, using reference points, resulted in deviations in the order of 0.1m, which is much more precise. The second method is therefore used. Still, deviations in the alignment might have influenced the results, although there are no specific cases found where this is expected.

Gridding

By using a grid, the number of points was reduced from roughly nine million to less than 50,000 points. Using a grid size of 1x1m, deformations of less than $1m^2$ may therefore be ignored. This limitation is not important for this thesis, as the anthropogenic deformations in this thesis are of higher order (>$20m^2$). However, another grid size might improve the results. For example, sudden height changes are emphasized more with smaller grid cells.

6.5. Limitations of the video data

In the video data, two data gaps were found. One data gap was in the period of February 24 to 25, 2020. The other was from February 26 until February 28, 2020. Deformations arising in these periods could therefore not be validated in the video data.

Another, fairly obvious limitation of the video data is the darkness during nighttime. Although some lights of the beach pavilion enlighten a small area, little can be seen. The formation of deformations during nighttime can therefore often not be seen in the video data. However, heavy equipment is not expected during nighttime, as driving and working in daylight might be preferred over driving and working in darkness.

Furthermore, the quality of the video data is limited by the weather. On clouded and rainy days, fewer details were visible in the video data. In some cases, even bulldozers could not be recognized in an image. On sunny days, the quality of the video data was higher, and objects of around 0.25m and larger could be recognized. Images showing the influence of the weather can be found in section 5.4.3.

In the video data, not every area is visible. In one case, no deformation cause could not be recognized, because a dune stood in front. In another case, the location of the deformation was out of view.

7

Conclusion and recommendations

In this chapter, an answer to the research question can be found in section 7.1. Recommendations for further research are made in section 7.2.

7.1. Conclusion

This thesis focuses on finding anthropogenic beach deformations, using the following research question:

> *How can anthropogenic beach deformations be characterized in laser data, using video data as validation?*

The answer to the research question is given in several parts, answering the four sub-questions given in chapter 1. First of all, the characteristics and limitations of the laser and video data are summarized (sub-question 2). Secondly, the method to filter out anthropogenic deformations in the laser data is explained briefly (sub-question 3). This method uses characteristics of the main deformation causes (sub-question 1). Finally, the results of the validation in the video data are summarized (sub-question 4).

In this thesis, laser and video data from a site in Noordwijk is used. The period of examination is from February 20 to April 26, 2020. The laser data has a data gap between April 5 to April 13. Other limitations of the laser data are invisible areas behind high objects and missing areas due to fog or rain. The video data is limited by two days of data gaps, darkness during nighttime, reduced quality during clouded days, reduced quality at larger distances, and invisible areas behind dunes and buildings.

The laser data is used to link deformations to human causes. Therefore, the laser data is first of all pre-processed, by selecting data, transforming, clipping, gridding and checking incomplete point clouds. Then, the height differences between every two consecutive days are visualised.

In a visual interpretation of these images, non-anthropogenic deformation causes are linked to deformation characteristics in the laser data. A decision tree is made to filter out deformations with non-anthropogenic causes, using the characteristics of deformation causes.

The characteristics of the main deformation causes are used in the decision tree. Sand waves are filtered out, using the characteristics >2000m^2 and a sand wave shape. Deformations due to erosion and sedimentation occur in the intertidal area and stretch more than 100m along the coast. Small deformations due to temporary presence of humans or vehicles are filtered out in two ways. Data sets with little deformations (<1% of area has more than 0.2m height difference) and deformations influencing a small area (<20m^2) are filtered out. From the results later on follows that erosion/sedimentation against buildings and freight containers is an important cause for beach deformations as well. This occurs at two specific locations next to freight containers.

In total, 30 deformations are not filtered out by the decision tree and are thus labeled as anthropogenic.

All 30 deformations that are labeled as anthropogenic in the laser data are validated in the video data. Validation in the video data shows 16 of these deformations have an anthropogenic cause, as a bulldozer is seen in the area of deformation.

With a success rate of 16 out of 30, the methodology to find anthropogenic beach deformations is proven successful. Furthermore, the results have provided more insight in deformation causes, which can be used to further increase the success rate.

7.2. Recommendations

By using the results of the initial decision tree, some improvements are recommended in the discussion section 6.3. Validation of the improvements can be done to check the functioning of the improved criteria and to further improve the methodology.

In general, it is recommended to use the decision tree on data from another period or at another location. In other data, other deformation causes might be present. Also, the values in the decision tree may vary per location, coördinate system and time period. This can lead to further improvements of the decision tree and more knowledge of the location and time period where beach deformations occur.

In this thesis, all deformations are manually checked with the decision tree. An improvement would be to automate this process. This should be possible for most criteria, as they are defined with values. However, a sand wave shape should be further defined when the decision tree is applied automatically. Automation could also be used to apply a ground filtering, to filter out any temporary deformation, like vehicles and human presence.

This thesis focuses on finding anthropogenic beach deformations, but the influence of these deformations on coastal protection is not examined yet. Further research on this topic is recommended to increase knowledge on the role of anthropogenic influences in coastal protection.

Bibliography

Aarninkhof, S., & Cohen, A. (2006). The advanced argus system. *Hydro International*, *10*(4), 38–41. www.scopus.com

AHN. (2022). *Ahn viewer*. Retrieved May 18, 2022, from https://www.ahn.nl/ahn-viewer

Anders, K., Lindenbergh, R. C., Vos, S. E., Mara, H., de Vries, S., & Höfle, B. (2019). High-frequency 3d geomorphic observation using hourly terrestrial laser scanning data of a sandy beach. *ISPRS Annals of the Photogrammetry, Remote Sensing and Spatial Information Sciences*, *IV-2/W5*, 317–324. https://doi.org/10.5194/isprs-annals-IV-2-W5-317-2019

Bogle, J., Bryan, K., Black, K., Hume, T., & Healy, T. (2001). Video observations of rip formation and evolution. *Journal of Coastal Research*, 117–127. https://www.jstor.org/stable/25736280

Boomaars, K. (2022). *Aeolian sand transport in noordwijk* (Master's thesis). TU Delft. the Netherlands.

Bosveld, E. (2020). *Influence of buildings on the aeolian sediment transport at the beach* (Bachelor's Thesis). TU Delft.

CBR. (2014). *Toeristische sector per gemeente, 2013*. Retrieved May 11, 2022, from https://www.cbs.nl/nl-nl/maatwerk/2014/10/toeristische-sector-per-gemeente-2013

de Vries, S., Southgate, H., Kanning, W., & Ranasinghe, R. (2012). Dune behavior and aeolian transport on decadal timescales. *Coastal Engineering*, *67*, 41–53. https://doi.org/10.1016/j.coastaleng.2012.04.002

Earth, G. (2022). *Noordwijk aan zee*. Retrieved May 11, 2022, from https://earth.google.com/web/

Eichmanns, C., & Schüttrumpf, H. (2021). Influence of sand trapping fences on dune toe growth and its relation with potential aeolian sediment transport. *Journal of Marine Science and Engineering*, *9*(8), 850. https://doi.org/10.3390/jmse9080850

Eitel, J. U., Höfle, B., Vierling, L. A., Abellán, A., Asner, G. P., Deems, J. S., Glennie, C. L., Joerg, P. C., LeWinter, A. L., Magney, T. S., Mandlburger, G., Morton, D. C., Müller, J., & Vierling, K. T. (2016). Beyond 3-d: The new spectrum of lidar applications for earth and ecological sciences. *Remote Sensing of Environment*, *186*, 372–392. https://doi.org/10.1016/j.rse.2016.08.018

Hage, P., Ruessink, B., & Donker, J. (2018). Determining sand strip characteristics using argus video monitoring. *Aeolian Research*, *33*, 1–11. https://doi.org/10.1016/j.aeolia.2018.03.007

Holman, R., Sallenger, A., Lippmann, T., & Haines, J. (1993). The application of video image processing to the study of nearshore processes. *Oceanography*, *6*(3), 78–85. https://doi.org/10.5670/oceanog.1993.02

Houthuys, R. (2012). *Morfologie van de vlaamse kust in 2011* (tech. rep.). Maritieme dienstverlening en Kust. Afdeling kust: Oostende.

Huguet, J.-R., Castelle, B., Marieu, V., Morichon, D., & de Santiago, I. (2016). Shoreline-sandbar dynamics at a high-energy embayed and structurally-engineered sandy beach: Anglet, SW france. *Journal of Coastal Research*, *75*(sp1), 393–397. https://doi.org/10.2112/si75-079.1

IPCC. (2021). *Climate change 2021: The physical science basis. contribution of working group i to the sixth assessment report of the intergovernmental panel on climate change*. Cambridge University Press. https://doi.org/10.1017/9781009157896.

Jin, J., Verbeurgt, J., Sloover, L. D., Stal, C., Deruyter, G., Montreuil, A.-L., Vos, S., Maeyer, P. D., & Wulf, A. D. (2021). Monitoring spatiotemporal variation in beach surface moisture using a long-range terrestrial laser scanner. *ISPRS Journal of Photogrammetry and Remote Sensing*, *173*, 195–208. https://doi.org/10.1016/j.isprsjprs.2021.01.011

Kuschnerus, M., Schröder, D., & Lindenbergh, R. (2021). Environmental influences on the stability of a permanently installed laser scanner. *The International Archives of the Photogrammetry, Remote Sensing and Spatial Information Sciences*, *XLIII-B2-2021*, 745–752. https://doi.org/10.5194/isprs-archives-XLIII-B2-2021-745-2021

Lazarus, E. D., & Goldstein, E. B. (2019). Is there a bulldozer in your model? *Journal of Geophysical Research: Earth Surface*, *124*(3), 696–699. https://doi.org/10.1029/2018jf004957

McNamara, D. E., & Werner, B. T. (2008). Coupled barrier island–resort model: 1. emergent instabilities induced by strong human-landscape interactions. *Journal of Geophysical Research*, *113*(F1). https://doi.org/10.1029/2007jf000840

Riegl. (2022). *Riegl vz-2000i*. Retrieved May 28, 2020, from http://www.riegl.com/nc/products/terrestrial-scanning/produktdetail/product/scanner/58/

Rijkswaterstaat. (2022). *Rijkswaterstaat waterinfo | waterhoogte astronomisch t.o.v. nap*. Retrieved May 11, 2022, from https://waterinfo.rws.nl/?#!/details/publiek/astronomische-getij/Scheveningen(SCHEVNGN)/Waterhoogte___20berekend___20Oppervlaktewater___20t.o.v.___20Normaal___20Amsterdams___20Peil___20in___20cm

Rogers, L. J., Moore, L. J., Goldstein, E. B., Hein, C. J., Lorenzo-Trueba, J., & Ashton, A. D. (2015). Anthropogenic controls on overwash deposition: Evidence and consequences. *Journal of Geophysical Research: Earth Surface*, *120*(12), 2609–2624. https://doi.org/10.1002/2015jf003634

Román-Rivera, M. A., Ellis, J. T., & Wang, C. (2020). Applying a rule-based object-based image analysis approach for nearshore bar identification and characterization. *Journal of Applied Remote Sensing*, *14*(04). https://doi.org/10.1117/1.jrs.14.044502

Schreijer, Y. (2021). *Visual insight into the temporal changes of sand patterns along the dutch coast* (Master's thesis). University Utrecht. the Netherlands.

Smit, M., Aarninkhof, S., Wijnberg, K., González, M., Kingston, K., Southgate, H., Ruessink, B., Holman, R., Siegle, E., Davidson, M., & Medina, R. (2007). The role of video imagery in predicting daily to monthly coastal evolution. *Coastal Engineering*, *54*(6-7), 539–553. https://doi.org/10.1016/j.coastaleng.2007.01.009

Strypsteen, G. (2019). *Monitoring and modelling aeolian sand transport at the belgian coast* (Doctoral dissertation). KU Leuven, Belgium.

Tiberius, C., van der Marel, H., Reudink, R., & van Leijen, F. (2021). *Surveying and mapping*. TU Delft OPEN. https://doi.org/https://doi.org/10.5074/T.2021.007

Vos, S., Lindenbergh, R., & de Vries, S. (2017). Coastscan: Continuous monitoring of coastal change using terrestrial laser scanning [Coastal Dynamics 2017 ; Conference date: 12-06-2017 Through 16-06-2017]. In T. Aagaard, R. Deigaard, & D. Fuhrman (Eds.), *Proceedings of coastal dynamics 2017* (pp. 1518–1528). http://coastaldynamics2017.dk

Vos, S., Spaans, L., Reniers, A., Holman, R., Mccall, R., & de Vries, S. (2020). Cross-shore intertidal bar behavior along the dutch coast: Laser measurements and conceptual model. *Journal of Marine Science and Engineering*, *8*, 864. https://doi.org/10.3390/jmse8110864

Vosselman, G., & Maas, H.-G. (2010). *Airborne and terrestrial laser scanning.* Whittles Publishing. https://doi.org/https://doi.org/10.5074/T.2021.007

A

Images resulting from video validation

A.1. Expected and found

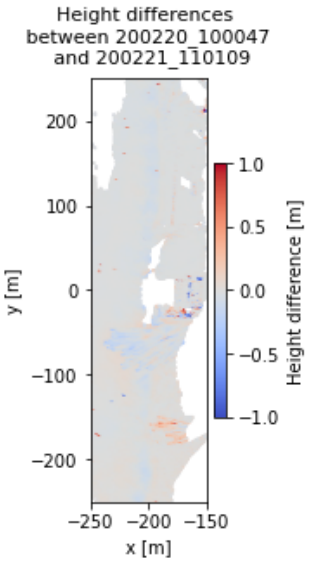

(a) Point cloud of the height differences over a time interval.

(b) A bulldozer is present in the area of deformation.

Figure A.1: Bulldozer on February 20th, afternoon around x=-220 and y=-50.

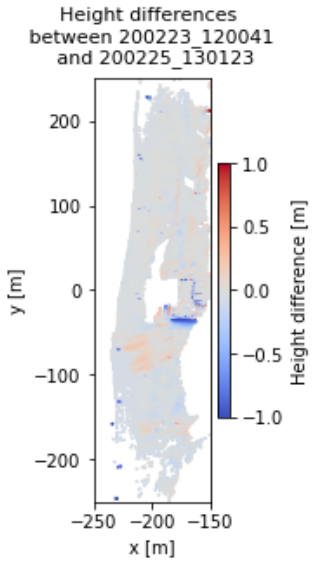

(a) Point cloud of the height differences over a time interval.

(b) A bulldozer is present just behind the dunes.

(c) A bulldozer is deposits sand just taken.

Figure A.2: Bulldozer on the morning of February 24, 2020 around x=-160 and y=-30 and x=-200 and y=-80.

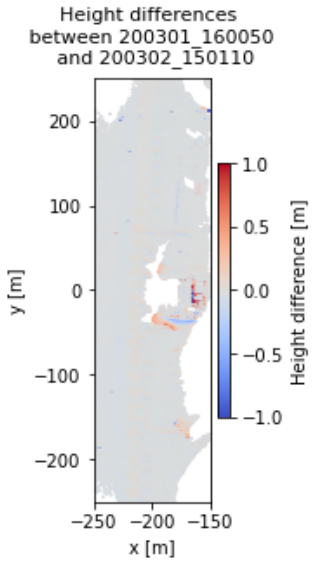

(a) Point cloud of the height differences over a time interval.

(b) A bulldozer is present in the area of deformation.

Figure A.3: Bulldozer on the morning of March 2, 2020 around x=-180 and y=-30.

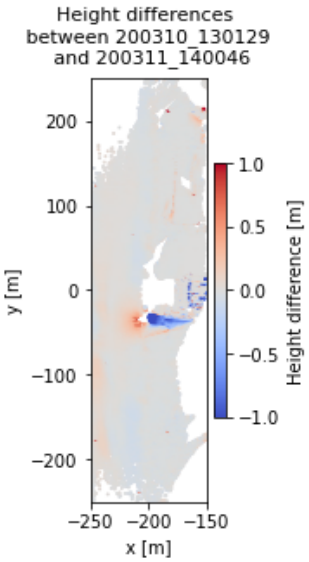

(a) Point cloud of the height differences over a time interval.

(b) A bulldozer is present and working in the area of deformation.

Figure A.4: Bulldozer on the afternoon of March 10, 2020 around x=-200 and y=-30.

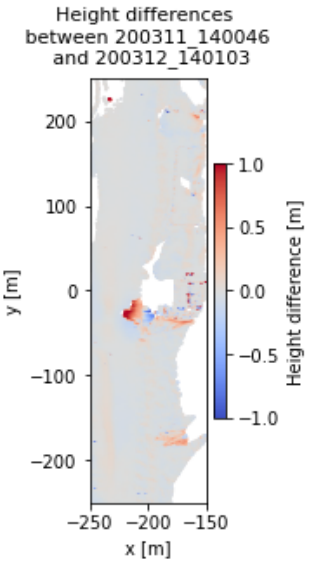

(a) Point cloud of the height differences over a time interval.

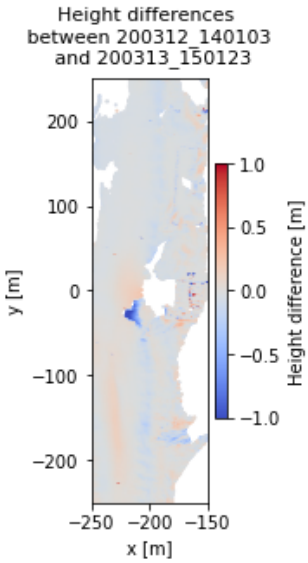

(b) Point cloud of the height differences over a time interval.

(c) A bulldozer is present and working in the afternoon of March 12, 2020 at the deformation of around x=-180 y=-180.

(d) A bulldozer is present and working in the afternoon of March 12, 2020 at the deformation of around x=-220 and y=-30.

Figure A.5: Bulldozers in the afternoon of March 12, 2020.

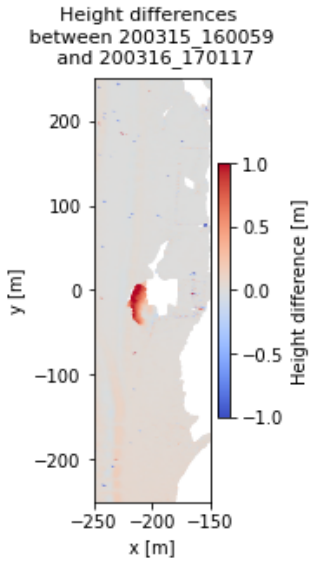

(a) Point cloud of the height differences over a time interval.

(b) A bulldozer is present in the area of deformation.

Figure A.6: Bulldozer on the morning of March 16, 2020 around x=-220 and y=-10.

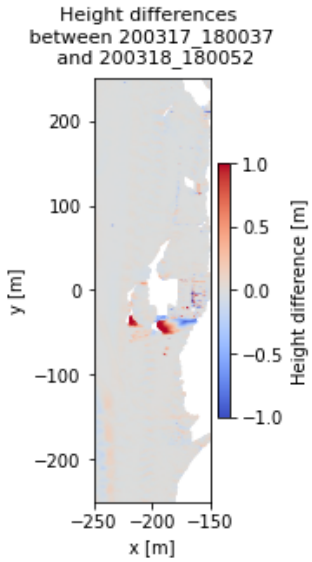

(a) Point cloud of the height differences over a time interval.

(b) A bulldozer is present in the area of deformation.

Figure A.7: Bulldozer on the afternoon of March 18, 2020 around x=-180 y=40 and x=-220 y=-10.

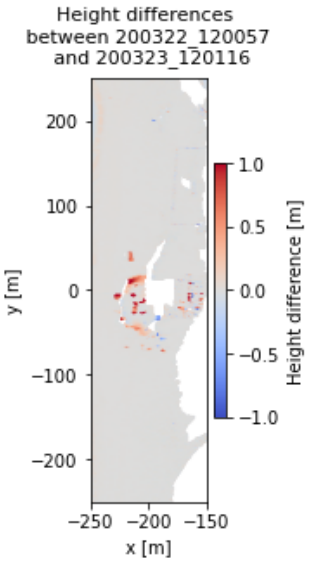

(a) Point cloud of the height differences over a time interval.

(b) Two bulldozers are present and working in the area of deformation.

Figure A.8: Two bulldozers on the morning of March 23, 2020 around x=-220 and -50<y<50.

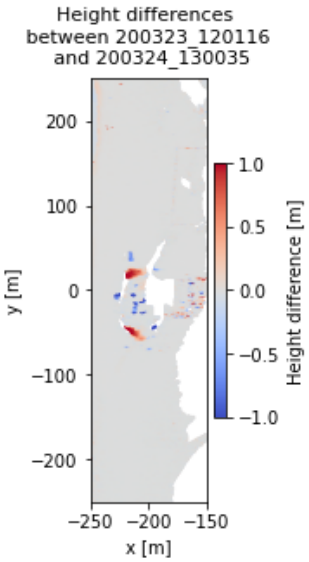

(a) Point cloud of the height differences over a time interval.

(b) A lot of heavy equipment is present and working in the area of deformation.

Figure A.9: A lot of heavy equipment on the afternoon of March 23, 2020 around x=-220 and -50<y<50.

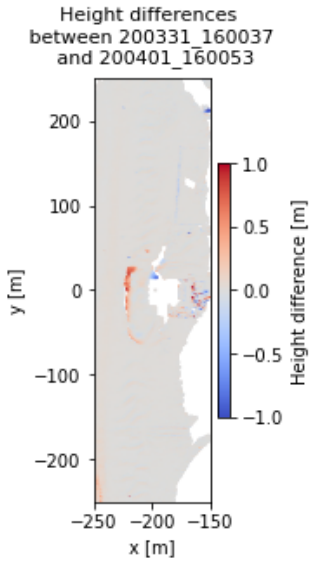

(a) Point cloud of the height differences over a time interval.

(b) A bulldozer is present in the area of deformation.

Figure A.10: Bulldozer on the afternoon of April 1, 2020 around x=-220 and -20<y<20.

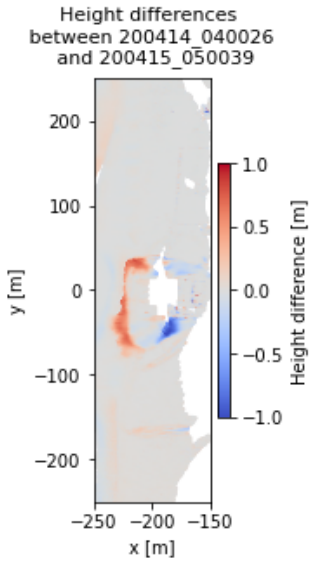

(a) Point cloud of the height differences over a time interval.

(b) Two bulldozer are present in the area of deformation.

Figure A.11: Two bulldozers in the morning of April 14, 2020 around x=-220 -50<y<30 and x=-180 y=-30.

A.2. Expected, not found

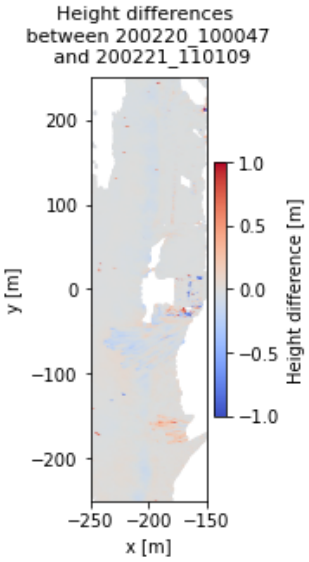

(a) Point cloud of the height differences over a time interval.

(b) Area of deformation around x=-180 y=-150 is not visible due to dunes.

Figure A.12: In the period February 20 to 21, the deformation around x=-180 y=-150 is not visible due to dunes.

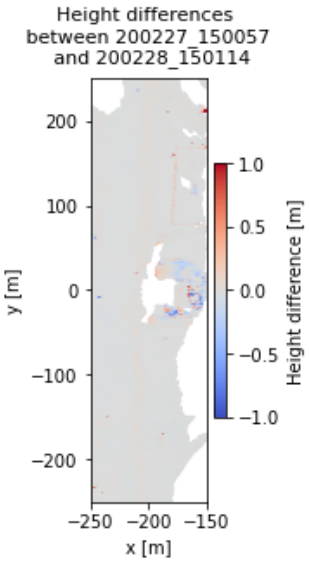

(a) Point cloud of the height differences over a time interval. Video data of this period is unavailable.

(b) Tyre tracks are visible on the morning of February 29, 2020.

Figure A.13: Video data unavailable in the period February 27 to 28, but tyre tracks are visible in the morning of February 29, 2020 around x=-180 y=30.

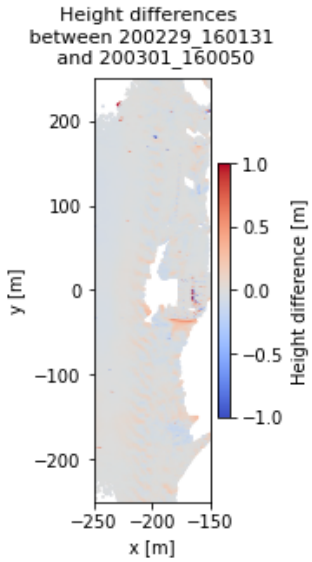

(a) Point cloud of the height differences over a time interval.

(b) Flags indicate a strong wind from the south, possibly causing sedimentation against the container.

(c) In the night, a light is seen temporarily near to the deformation.

Figure A.14: No bulldozers are seen between February 29 and March 1 around x=-180 y=-30 (location of container). The video data shows two possible explanations for the deformation: wind causes sedimentation or a nightly light is the sign of anthropogenic deformation.

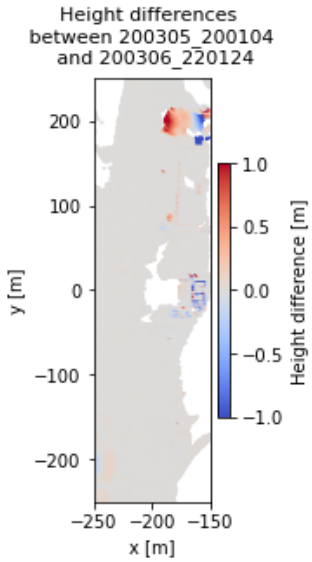

(a) Point cloud of the height differences over a time interval.

(b) A bulldozer is seen. However, the area of deformation (x=-180, y=200) is more to the right, and is not visible in the video data.

Figure A.15: In the period March 5 to 6, 2020, the deformation of x=-180, y=200 lies outside the visible area of the video data.

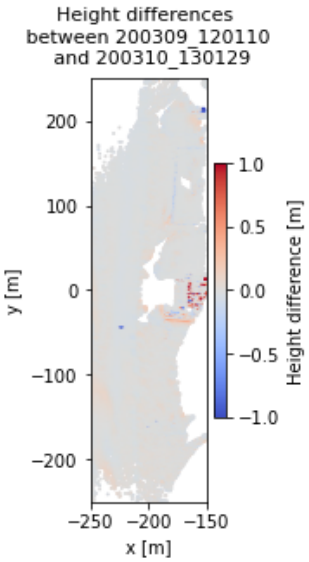

(a) Point cloud of the height differences over a time interval.

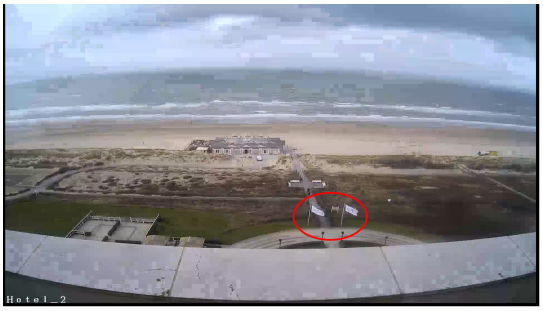

(b) Flags indicate a strong wind from the south, possibly causing sedimentation against the container.

Figure A.16: In the period March 9 to 10, 2020, the deformation of x=-180, y=-30 might be caused by sedimentation due to a strong wind from the south, indicated by the flags visible in the video data.

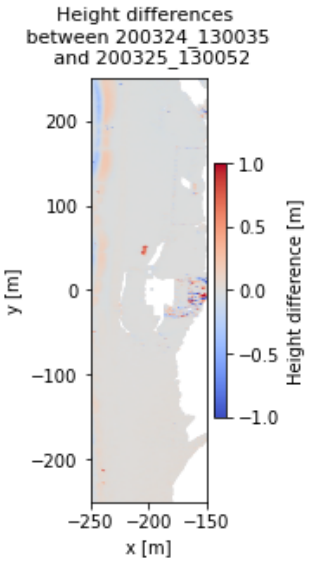

(a) Point cloud of the height differences over a time interval.

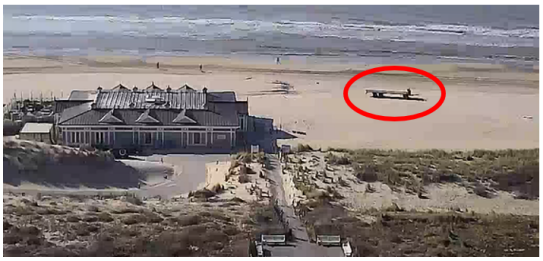

(b) A vehicle is placed on the beach, at the location of the deformation.

Figure A.17: In the period March 24 to 25, 2020, a vehicle is placed on the beach, causing a deformation at x=-210, y=50.

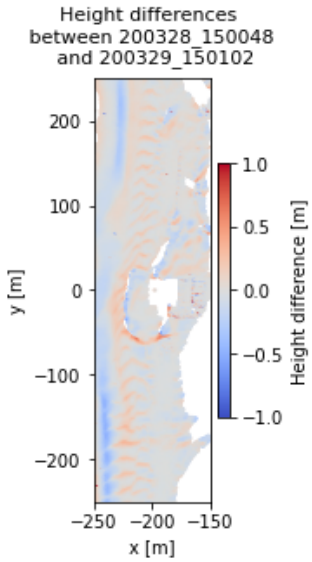

(a) Point cloud of the height differences over a time interval.

(b) High tide in the period March 28 to 29. The deformation in the area x=-220 and -20<y<20 might be caused by erosion and sedimentation.

(c) Before possible human intervention.

(d) Possibly, human intervention is visible in this image at the location of deformation.

Figure A.18: In the period March 28 to 29, 2020, the quality of the video data is low. Still, anthropogenic influence might be visible around x=-220,-20<y<20. Another cause for this deformation can be erosion and sedimentation.

A.3. Unexpected and found

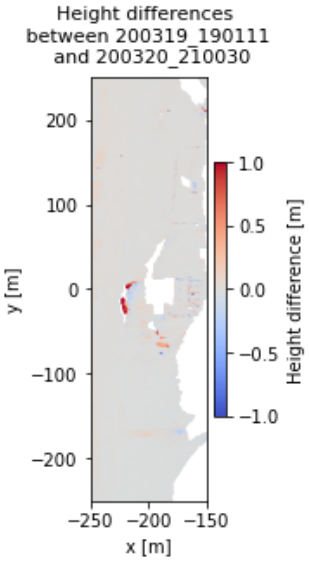

(a) Point cloud of the height differences over a time interval.

(b) A bulldozer is working and causing a deformation around x=-220 and y=0.

Figure A.19: A bulldozer is working and causing a deformation in the time interval March 19 to 20. The point cloud was filtered out as less than 1% of the area had deformations outside the thresholds of -0.2 and +0.2 [m].

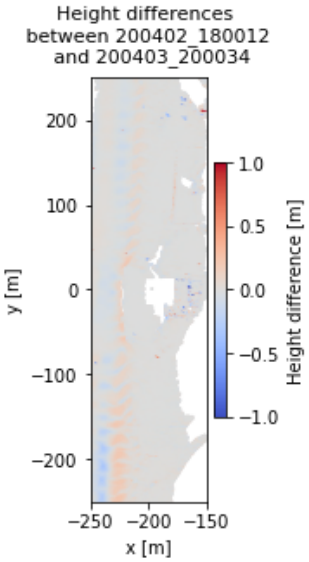

(a) Point cloud of the height differences over a time interval.

(b) A bulldozer is visible and seems to replace waste bins.

Figure A.20: A bulldozer seems to replace waste bins on the morning of April 3, 2020. The resulting deformation in the point cloud is negligible (<20[m^2]).

A.4. Check sand waves and vehicles

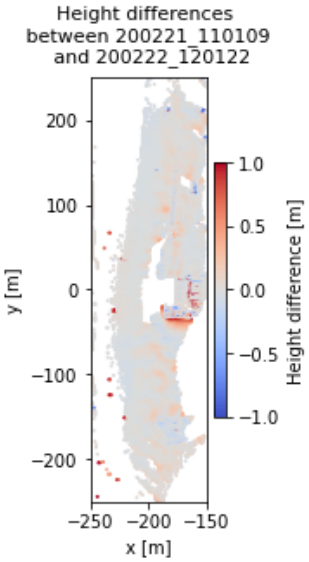

(a) Point cloud of the height differences over a time interval.

(b) Sand waves visible on February 22, 2020.

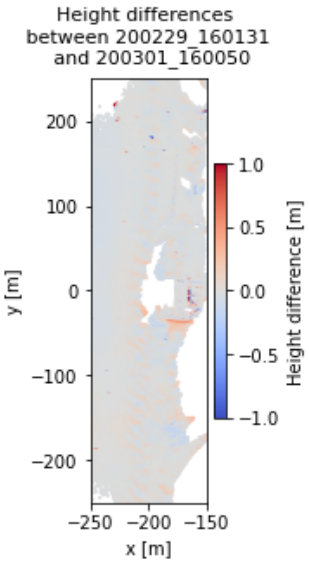

(c) Point cloud of the height differences over a time interval.

(d) Sand waves visible on the morning of March 1, 2020.

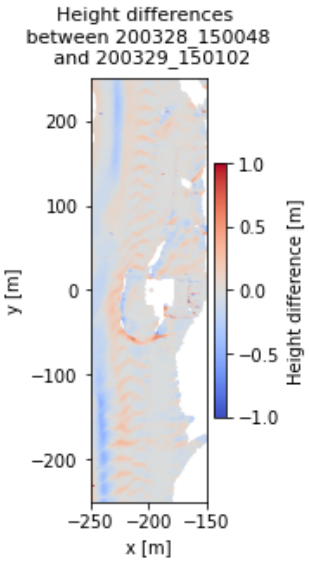

(e) Point cloud of the height differences over a time interval.

(f) Sand waves visible on March 29, 2020.

Figure A.21: Validation check in video data of sand waves. Three point clouds where sand waves were recognized are checked.

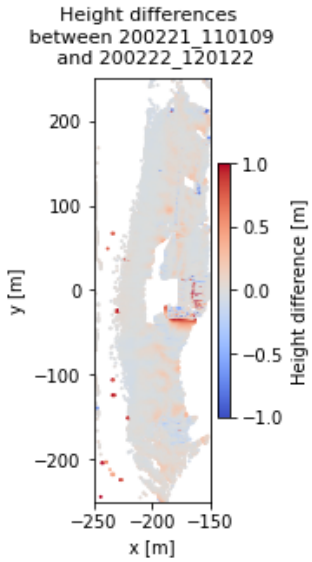

(a) Point cloud of the height differences over a time interval.

(b) Bus in front of restaurant on February 21, 2020.

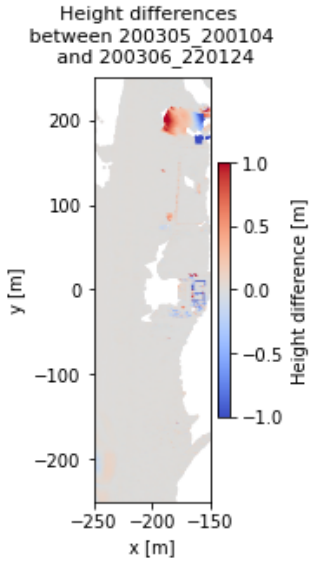

(c) Point cloud of the height differences over a time interval.

(d) A loading truck in front of restaurant on March 6, 2020.

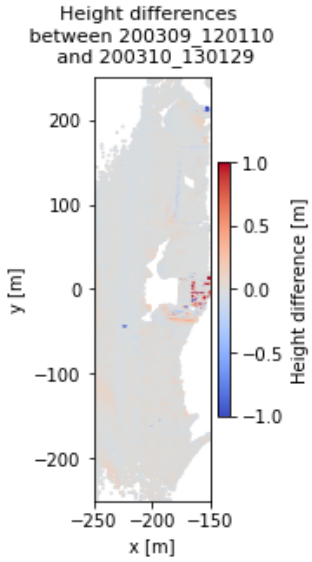

(e) Point cloud of the height differences over a time interval.

(f) Vehicle in front of restaurant on March 9, 2020.

Figure A.22: The area -180<x<-150 and -30<y<30 contains many small deformations. Cars, buses and trucks are often the cause of these small deformations.

A.5. Low image quality

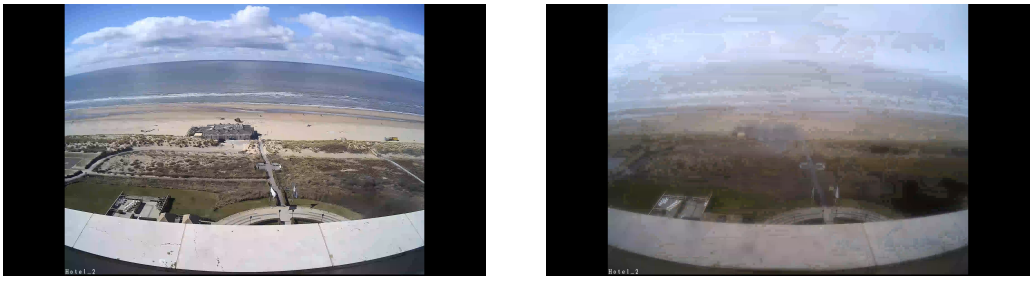

(a) High image quality on April 1, 2020.

(b) Very low image quality on March 30, 2020.

Figure A.23: The image quality is dependant on the weather. The image quality is lower on cloudy, rainy days.

B

Python script

In [1]:

```
import pandas as pd
import numpy as np
import matplotlib.pyplot as plt

from os import  listdir,path
import laspy
import time
```

Determine boundaries

In this cell the boundaries of the used area are displayed.

In [2]:

```
z_scanner = 55.755   # scanner elevation in m (compared to NAP)
min_elev = -10 #-30  # min z value to remove outliers at low elevations
max_elev = 22    # max z value needed in data in m compared to ground level
min_x = -250         # min x value
max_x = -150         # Filter out dune area  # max x-coordinate of -50  to filter out p
oints on hotel terrace, for filter out dune are use -150
min_y = -250         # for now, only the y-values around the beach club are chosen
max_y = 250
filepath = 'C:/Users/Debora/Documents/Civiel/3.4 BEP/Data/LaserLowTides/'  # dit nog ov
eral invoeren
```

Make dataframe

The next cell makes a dataframe with all possible x and y values in a grid, with cells of 1x1m. This data_grid dataframe is later used to store the heights of the points at certain moments.

In [3]:

```
  # creating df grid
def make_grid_file(min_x, max_x, min_y, max_y):
    x = np.linspace(min_x+1, max_x, max_x-min_x) # make list of x-values within boundar
ies, having a step size of 1
    y = np.linspace(min_y+1, max_y, max_y-min_y) # make list of y-values within boundar
ies, having a step size of 1

    len_list = len(x) * len(y)   # List has to be no. of x-values times no. of y-values
    x_list = np.zeros(len_list)
    y_list = np.zeros(len_list)
    for i in range(len(x)):      # x ascends for a y-value, then take next y-value and
 ascend x again. In that way, fill the dataframe
        for j in range(len(y)):
            index = i + j*len(x)
            x_list[index] = x[i]
            y_list[index] = y[j]

    data_grid = pd.DataFrame({'x' : x_list, 'y' : y_list})  # make a dataframe of the v
alues
    data_grid.to_csv('C:/Users/Debora/Documents/Civiel/3.4 BEP/Data/LaserLowTides/x'
                     + str(min_x) + ',' + str(max_x) + ';y_' + str(min_y) + ',' + str(m
ax_y) +
                     '_grid.csv', index=False, header=True) # save dataframe to a .csv
 file, having the x- and y-boundaries in the filename
    return data_grid

make_grid_file(min_x, max_x, min_y, max_y)
```

Out[3]:

	x	y
0	-249.0	-249.0
1	-248.0	-249.0
2	-247.0	-249.0
3	-246.0	-249.0
4	-245.0	-249.0
...	...	...
49995	-154.0	250.0
49996	-153.0	250.0
49997	-152.0	250.0
49998	-151.0	250.0
49999	-150.0	250.0

50000 rows × 2 columns

Function to load data

This function does a lot of things:

- it loads the data
- it filters out z-values
- it transforms the data, using the matrix transformation file of that moment
- then it corrects for the hotel height, to NAP values
- it sets boundaries for x and y
- it makes whole numbers of x and y values, and takes the average value per grid cell (so 1x1m)
- it saves the average z-values in a .csv file

In [4]:

```
def store_to_grid_file(filename_laz, read_refl=False,   # Note: this function takes qui
te some time
                       min_elev = -10, max_elev = 10, min_x = -250, max_x = -150, min_y
= -100, max_y = 100):

 # Read .laz file
    if '.laz' in filename_laz:
        inFile = laspy.read(filename_laz)
        data = pd.DataFrame({'x' : np.array(inFile.x), 'y' : np.array(inFile.y), 'z' :n
p.array(inFile.z)})

        if read_refl:
            reflectance = inFile.points["point"]["reflectance"] * inFile.header.vlrs[0]
.reflectance.scale[0]
            data['ref'] = reflectance

    else:
        raise ValueError('unknown file format:'+filename_laz)


 # Use boundaries in z direction
    z_scanner = 55.755   # scanner elevation in m (compared to NAP)
    data = data[data.z <= max_elev-z_scanner]
    data = data[data.z >= min_elev-z_scanner]

 # Rotate, use matrix from .tlaz files
    if not 'aligned' in filename_laz:
    # rotate data to correct for inclination:
        trafomat_file = filename_laz[:-4]+'_trafomat.tlaz'
        if path.isfile(trafomat_file):
            trafomat = np.loadtxt(trafomat_file)
            rotation = np.array(trafomat)[:, :3]
            translation = np.array(trafomat)[:, 3].flatten()

            pts_rot = data.dot(rotation.T)
            pts_trafo = pts_rot + translation

            data.x = pts_trafo[0]
            data.y = pts_trafo[1]
            data.z = pts_trafo[2]

        else:
            print('Rotation file not found!')


 # correct for scanner height, so that z-coordinate corresponds to NAP and is not negat
ive
    data.z = data.z + z_scanner

 # filter out area
    data = data[data.x <= max_x]
    data = data[data.x >= min_x]
    data = data[data.y <= max_y]
    data = data[data.y >= min_y]

 # Reduce number of points by taking the average of every square meter
    data = data.round({'x':0, 'y':0})  # rounding all numbers to whole numbers
    data = data.groupby(['x', 'y'], as_index=False)['z'].mean()  # sort data by x and
 y, then take the average height of every grid cell
```

```
 # Save averaged z-values in dataframe of grid

    filename_csv = f'C:/Users/Debora/Documents/Civiel/3.4 BEP/Data/LaserLowTides/x{min_
x},{max_x};y_{min_y},{max_y}_grid.csv'
    data_grid = pd.read_csv(filename_csv)  # Read .csv file of grid

    data_grid['z'] = np.nan * np.ones(len(data_grid.x)) # make new column for z-values
    for i in range (len(data.z)):
        data_grid.z[(data.x[i] == data_grid.x) & (data.y[i] == data_grid.y)] = data.z[i
]  # assign z-value to correct row in grid dataframe

    datetime = filename_laz[-17:-4]    # take date_time from filename
    data_grid.z.to_csv(f'C:/Users/Debora/Documents/Civiel/3.4 BEP/Data/LaserLowTides/{d
atetime}_trafomatrix_gridded.csv', index=False, header=True)

 # output line
    print(f'{len(data.z)} vales of date and time {datetime} have been added to the grid
{min_x, max_x, min_y, max_y} file')

    return data
```

In [5]:

```
# This cell uses the function on data of dates_to_load. Note that this can take about 1
0 minutes per date.
# Note that the date-time format is YYMMDD_HHMMSS (year month day _ hour minutes second
s)

dates_loaded = ['200220_100047', '200221_110109', '200222_120122', '200223_120041',
                '200224_120059', '200225_130123', '200226_140138', '200227_150057',
                '200228_150114', '200229_160131',
                '200301_160050', '200302_150110', '200303_160126', '200304_190046',
                '200305_200104', '200306_220124', '200307_230042', '200308_110051',
                '200309_120110', '200310_130129', '200311_140046', '200312_140103',
                '200313_150123', '200314_160041', '200315_160059', '200316_170117',
                '200317_180037', '200318_180052', '200319_190111', '200320_210030',
                '200321_110039', '200322_120057', '200323_120116', '200324_130035',
                '200325_130052', '200326_140110', '200327_140027', '200328_150048',
                '200329_150102', '200330_160019', '200331_160037',
                '200401_160053', '200402_180012', '200403_200034', '200404_210052',
                '200405_110100',
                '200413_160113', '200414_040026', '200415_050039', '200416_050057',
                '200417_060019', '200418_080035', '200419_100053', '200420_110012',
                '200421_120028', '200422_120046', '200423_120003', '200424_130024',
                '200425_130038', '200426_135955']  # don't use these anymore, its alrea
dy loaded
nog_laden = []
dates_to_load = []

for i in range (len(dates_to_load)):
    filename_laz = filepath+dates_to_load[i]+'.laz'
    print(filename_laz)
    store_to_grid_file(filename_laz, min_elev=min_elev, max_elev=max_elev, min_x=min_x,
max_x=max_x, min_y=min_y, max_y=max_y)
    #store_to_grid_file(filename_laz)  # in smaller area automatically x (-250, -150) y
(-100, 100)
```

Storing data in matrices (dataframes)

- in the first cell, the general grid is filled with columns of the loaded dates
- in the second cell, the area percentage where the height difference is below -0.2m, between -0.2 and +0.2m, and above +0.2m is determined per time interval.

In [6]:

```
  # load grid file and add height columns
dates_loaded = []  # don't use these anymore, its already done
dates_to_grid = ['200220_100047', '200221_110109', '200222_120122', '200223_120041',
                 '200224_120059', '200225_130123', '200226_140138', '200227_150057',
                 '200228_150114', '200229_160131',
                 '200301_160050', '200302_150110', '200303_160126', '200304_190046',
                 '200305_200104', '200306_220124', '200307_230042', '200308_110051',
                 '200309_120110', '200310_130129', '200311_140046', '200312_140103',
                 '200313_150123', '200314_160041', '200315_160059', '200316_170117',
                 '200317_180037', '200318_180052', '200319_190111', '200320_210030',
                 '200321_110039', '200322_120057', '200323_120116', '200324_130035',
                 '200325_130052', '200326_140110', '200327_140027', '200328_150048',
                 '200329_150102', '200330_160019', '200331_160037',
                 '200401_160053', '200402_180012', '200403_200034', '200404_210052',
                 '200405_110100',
                 '200413_160113', '200414_040026', '200415_050039', '200416_050057',
                 '200417_060019', '200418_080035', '200419_100053', '200420_110012',
                 '200421_120028', '200422_120046', '200423_120003', '200424_130024',
                 '200425_130038', '200426_135955' ]  # make sure these dates passed the
 cell above

data_grid = pd.read_csv(f'C:/Users/Debora/Documents/Civiel/3.4 BEP/Data/LaserLowTides/x
{min_x},{max_x};y_{min_y},{max_y}_grid.csv')
for i in range(len(dates_to_grid)):

     # find correct file
    path = filepath
    date = dates_to_grid[i]
    gridsize = '_x'+str(min_x) + ',' + str(max_x) + ';y' + str(min_y) + ',' + str(max_y
)
    filename = path+date+'_trafomatrix_gridded.csv'

     # add height data to grid dataframe
    data_grid['z_'+date] = pd.read_csv(filename)

display(data_grid)
```

	x	y	z_200220_100047	z_200221_110109	z_200222_120122	z_200223_120041
0	-249.0	-249.0	5.536735	NaN	NaN	NaN
1	-248.0	-249.0	5.554748	NaN	NaN	NaN
2	-247.0	-249.0	5.566946	NaN	NaN	NaN
3	-246.0	-249.0	5.570162	NaN	NaN	NaN
4	-245.0	-249.0	5.586246	5.608082	NaN	NaN
...	...	...	...	...	...	...
49995	-154.0	250.0	NaN	4.262577	4.448565	NaN
49996	-153.0	250.0	4.319043	5.093514	4.424272	NaN
49997	-152.0	250.0	4.421943	4.414834	NaN	NaN
49998	-151.0	250.0	4.456762	4.454656	NaN	NaN
49999	-150.0	250.0	NaN	NaN	NaN	NaN

50000 rows × 62 columns

In [7]:

```
columns_to_use = ['200220_100047', '200221_110109', '200222_120122', '200223_120041',
#'200224_120059',]
                          '200225_130123', '200226_140138', '200227_150057',
                          '200228_150114', '200229_160131',
                          '200301_160050', '200302_150110', '200303_160126', '200304_1900
46',
                          '200305_200104', '200306_220124', '200307_230042', '200308_1100
51',
                          '200309_120110', '200310_130129', '200311_140046', '200312_1401
03',
                          '200313_150123', '200314_160041', '200315_160059', '200316_1701
17',
                          '200317_180037', '200318_180052', '200319_190111', '200320_2100
30',
                          '200321_110039', '200322_120057', '200323_120116', '200324_1300
35',
                          '200325_130052', '200326_140110', '200327_140027', '200328_1500
48',
                          '200329_150102', '200330_160019', '200331_160037',
                          '200401_160053', '200402_180012', '200403_200034', '200404_2100
52',
                          '200405_110100',
                          '200413_160113', '200414_040026', '200415_050039', '200416_0500
57',
                          '200417_060019', '200418_080035', '200419_100053', '200420_1100
12',
                          '200421_120028', '200422_120046', '200423_120003', '200424_1300
24',
                          '200425_130038', '200426_135955' ]
date_from = np.zeros(len(columns_to_use)-1)
date_to = np.zeros(len(columns_to_use)-1)
grid_cells = np.zeros(len(columns_to_use)-1)

perc_left = np.zeros(len(columns_to_use)-1)
perc_mid = np.zeros(len(columns_to_use)-1)
perc_right = np.zeros(len(columns_to_use)-1)

threshold = .2

for i in range(len(columns_to_use)-1):  # loop through all time intervals
        name1 = 'z_'+columns_to_use[i]    # first date name
        name2 = 'z_'+columns_to_use[i+1]  # second date name
        delta_z = data_grid[name2] - data_grid[name1]

        delta_z = delta_z[~np.isnan(delta_z)]  # filter out Not a Number values
        z_left = delta_z[delta_z <= -threshold]
        z_mid = delta_z[(delta_z > -threshold) & (delta_z < threshold)]
        z_right = delta_z[delta_z >= threshold]

        date_from[i] = columns_to_use[i][0:6]
        date_to[i] = columns_to_use[i+1][0:6]
        grid_cells[i] = len(delta_z)
        perc_left[i] = len(z_left) / len(delta_z) * 100
        perc_mid[i] = len(z_mid) / len(delta_z) * 100
        perc_right[i] = len(z_right) / len(delta_z) * 100

datadiff = pd.DataFrame({'from date' : date_from.round(decimals=0), 'to date' : date_to
, 'filled gridcells': grid_cells,
                         'below lower bound': perc_left.round(decimals=2), 'within thre
```

```
sholds': perc_mid.round(decimals=2),
                        'above upper bound': perc_right.round(decimals=2), 'total outs
ide thresholds': perc_left.round(decimals=2)+perc_right.round(decimals=2)})
#datadiff.sort_values('total outside thresholds', inplace=True, ascending=False)  # can
be used to put highest percentage outside thresholds on top
datadiff.to_excel(filepath+'output.xlsx')
display(datadiff)
```

	from date	to date	filled gridcells	below lower bound	within thresholds	above upper bound	total outside thresholds
0	200220.0	200221.0	38248.0	0.59	98.57	0.84	1.43
1	200221.0	200222.0	21334.0	0.66	96.48	2.85	3.51
2	200222.0	200223.0	19103.0	0.37	98.26	1.37	1.74
3	200223.0	200225.0	21539.0	1.99	97.08	0.92	2.91
4	200225.0	200226.0	38534.0	0.43	99.31	0.26	0.69
5	200226.0	200227.0	39721.0	0.38	98.85	0.77	1.15
6	200227.0	200228.0	40387.0	0.64	98.88	0.48	1.12
7	200228.0	200229.0	40389.0	0.35	99.36	0.29	0.64
8	200229.0	200301.0	39233.0	0.35	98.89	0.76	1.11
9	200301.0	200302.0	38827.0	0.48	98.80	0.72	1.20
10	200302.0	200303.0	39710.0	0.27	99.53	0.20	0.47
11	200303.0	200304.0	41095.0	0.28	99.42	0.31	0.59
12	200304.0	200305.0	39040.0	0.34	99.28	0.38	0.72
13	200305.0	200306.0	38774.0	0.85	97.32	1.83	2.68
14	200306.0	200307.0	41424.0	0.19	99.61	0.20	0.39
15	200307.0	200308.0	41349.0	0.22	99.45	0.33	0.55
16	200308.0	200309.0	41388.0	0.43	99.28	0.29	0.72
17	200309.0	200310.0	34030.0	0.34	98.97	0.68	1.02
18	200310.0	200311.0	34034.0	1.45	97.15	1.41	2.86
19	200311.0	200312.0	39245.0	0.43	97.58	1.99	2.42
20	200312.0	200313.0	38543.0	1.41	98.08	0.51	1.92
21	200313.0	200314.0	39844.0	0.32	99.07	0.60	0.92
22	200314.0	200315.0	41817.0	0.47	99.20	0.33	0.80
23	200315.0	200316.0	41679.0	0.24	98.62	1.14	1.38
24	200316.0	200317.0	41751.0	0.25	99.59	0.16	0.41
25	200317.0	200318.0	41388.0	0.71	98.21	1.07	1.78
26	200318.0	200319.0	41541.0	0.17	99.63	0.20	0.37
27	200319.0	200320.0	41399.0	0.30	99.20	0.50	0.80
28	200320.0	200321.0	41508.0	0.15	99.70	0.15	0.30
29	200321.0	200322.0	41480.0	0.16	99.64	0.20	0.36
30	200322.0	200323.0	41269.0	0.22	98.55	1.22	1.44
31	200323.0	200324.0	41193.0	0.60	98.40	1.00	1.60
32	200324.0	200325.0	41390.0	1.10	98.03	0.87	1.97
33	200325.0	200326.0	41321.0	1.07	97.92	1.01	2.08
34	200326.0	200327.0	41272.0	0.51	99.06	0.43	0.94
35	200327.0	200328.0	41215.0	0.24	99.50	0.26	0.50
36	200328.0	200329.0	41134.0	4.95	92.74	2.31	7.26

	from date	to date	filled gridcells	below lower bound	within thresholds	above upper bound	total outside thresholds
37	200329.0	200330.0	41736.0	0.38	99.04	0.58	0.96
38	200330.0	200331.0	41849.0	0.22	99.58	0.20	0.42
39	200331.0	200401.0	41283.0	0.37	98.71	0.92	1.29
40	200401.0	200402.0	41113.0	0.48	99.28	0.24	0.72
41	200402.0	200403.0	41291.0	0.69	98.83	0.48	1.17
42	200403.0	200404.0	41540.0	0.09	99.82	0.08	0.17
43	200404.0	200405.0	41697.0	0.14	99.67	0.19	0.33
44	200405.0	200413.0	40914.0	3.07	92.39	4.54	7.61
45	200413.0	200414.0	41029.0	0.12	99.39	0.49	0.61
46	200414.0	200415.0	41315.0	1.25	95.81	2.95	4.20
47	200415.0	200416.0	41619.0	0.12	99.70	0.18	0.30
48	200416.0	200417.0	41617.0	0.19	99.64	0.17	0.36
49	200417.0	200418.0	41714.0	0.15	99.73	0.12	0.27
50	200418.0	200419.0	41688.0	0.11	99.76	0.13	0.24
51	200419.0	200420.0	41706.0	0.18	99.53	0.29	0.47
52	200420.0	200421.0	41706.0	0.44	99.21	0.35	0.79
53	200421.0	200422.0	41790.0	0.13	99.65	0.21	0.34
54	200422.0	200423.0	41758.0	0.22	99.56	0.22	0.44
55	200423.0	200424.0	41735.0	0.21	99.52	0.27	0.48
56	200424.0	200425.0	41544.0	0.55	99.19	0.26	0.81
57	200425.0	200426.0	41592.0	0.27	99.48	0.25	0.52

Plotting the data

- first, the point clouds are displayed to find disturbed point clouds
- in the next cell, the height differences are plotted
- the third cell contains code to plot the height difference in point clouds and histograms

In [8]:

```
# In this cell, the point clouds of every day are plotted
dates_to_display = ['200220_100047', '200221_110109', '200222_120122', '200223_120041',
'200224_120059',
                '200225_130123', '200226_140138', '200227_150057',
                '200228_150114', '200229_160131',
                '200301_160050', '200302_150110', '200303_160126', '200304_190046',
                '200305_200104', '200306_220124', '200307_230042', '200308_110051',
                '200309_120110', '200310_130129', '200311_140046', '200312_140103',
                '200313_150123', '200314_160041', '200315_160059', '200316_170117',
                '200317_180037', '200318_180052', '200319_190111', '200320_210030',
                '200321_110039', '200322_120057', '200323_120116', '200324_130035',
                '200325_130052', '200326_140110', '200327_140027', '200328_150048',
                '200329_150102', '200330_160019', '200331_160037',
                '200401_160053', '200402_180012', '200403_200034', '200404_210052',
                '200405_110100',
                '200413_160113', '200414_040026', '200415_050039', '200416_050057',
                '200417_060019', '200418_080035', '200419_100053', '200420_110012',
                '200421_120028', '200422_120046', '200423_120003', '200424_130024',
                '200425_130038', '200426_135955']

n = len(dates_to_display)      # number of dates to load
n_row = 8
n_hor = int(n / n_row)          # calculate number of pictures on a row and make an int
eger of it
norm = plt.Normalize(-0,12)     # set range of 0 to 12 m height

fig, axes = plt.subplots(nrows=n_row, ncols=n_hor, figsize=(20,50), sharey=True)
for i in range(n_row):
    for j in range(n_hor):
        index = j + i*n_hor
        name = 'z_' + dates_to_display[index]
        column_data = data_grid[name]

        pcm = axes[i, j].scatter(x=data_grid.x, y=data_grid.y, c=column_data, s=1, cmap
='viridis', norm=norm)
        axes[i, j].set_xlim([min_x, max_x])
        axes[i, j].set_ylim([min_y, max_y])
        axes[i, j].set_title(name)

fig.colorbar(pcm, ax=axes[:, :], location='right', shrink=0.6)
plt.show()
plt.tight_layout()
fig.savefig(filepath+'z_all.png', bbox_inches = "tight");
```

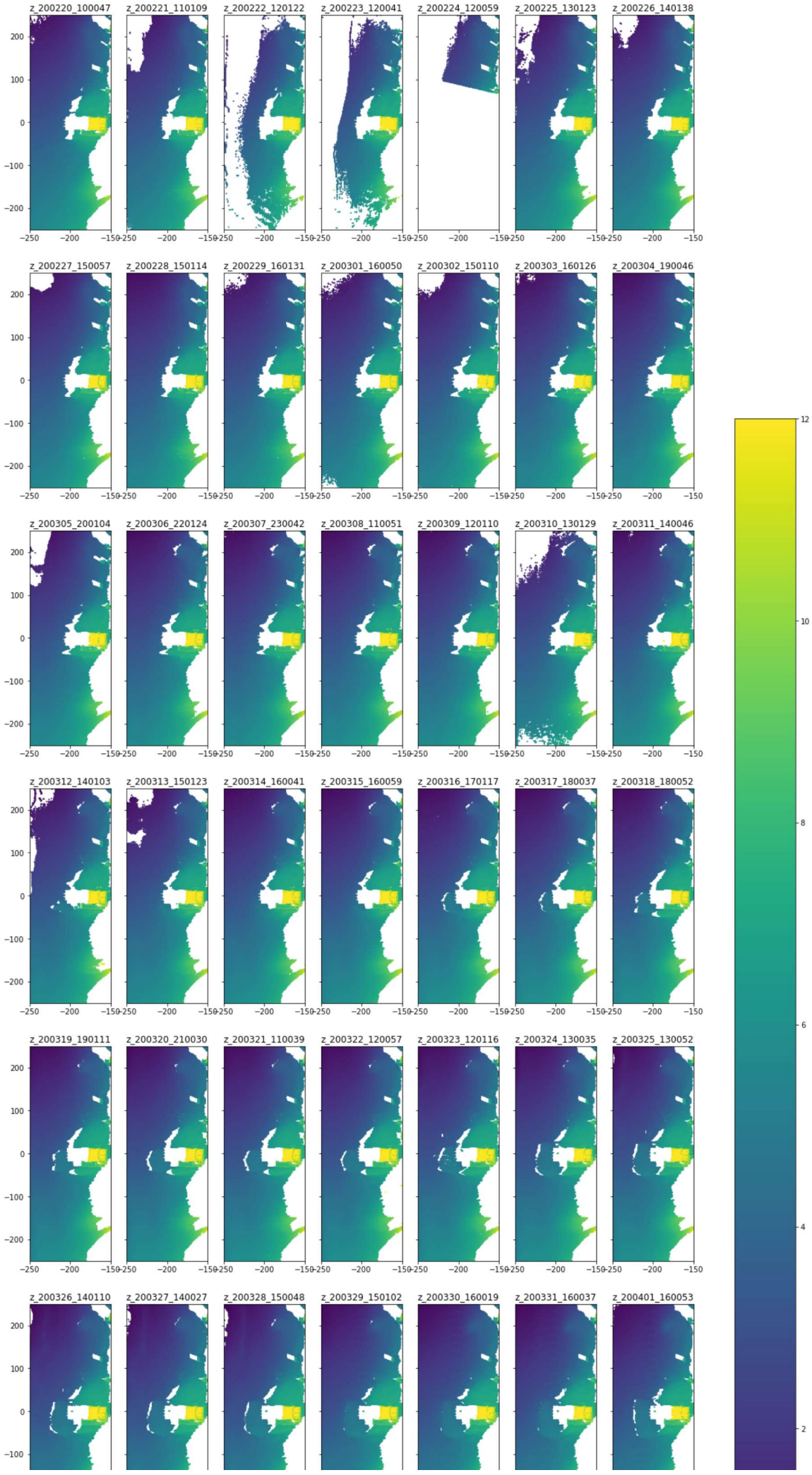
z_200220_100047
z_200221_110109
z_200222_120122
z_200223_120041
z_200224_120059
z_200225_130123
z_200226_140138
z_200227_150057
z_200228_150114
z_200229_160131
z_200301_160050
z_200302_150110
z_200303_160126
z_200304_190046
z_200305_200104
z_200306_220124
z_200307_230042
z_200308_110051
z_200309_120110
z_200310_130129
z_200311_140046
z_200312_140103
z_200313_150123
z_200314_160041
z_200315_160059
z_200316_170117
z_200317_180037
z_200318_180052
z_200319_190111
z_200320_210030
z_200321_110039
z_200322_120057
z_200323_120116
z_200324_130035
z_200325_130052
z_200326_140110
z_200327_140027
z_200328_150048
z_200329_150102
z_200330_160019
z_200331_160037
z_200401_160053

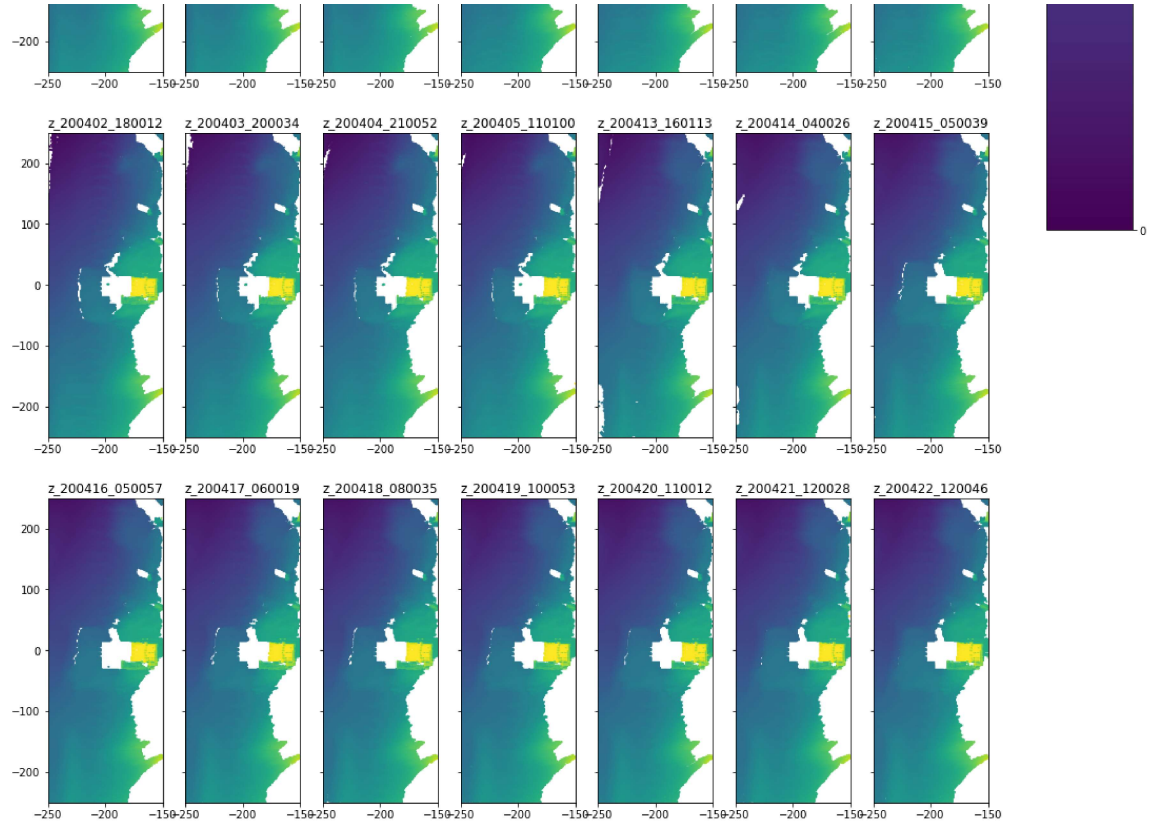

<Figure size 432x288 with 0 Axes>

In [9]:

```
columns_to_display = ['200220_100047', '200221_110109', '200222_120122', '200223_12004
1', #'200224_120059',
                '200225_130123', '200226_140138', '200227_150057',
                '200228_150114', '200229_160131',
                '200301_160050', '200302_150110', '200303_160126', '200304_190046',
                '200305_200104', '200306_220124', '200307_230042', '200308_110051',
                '200309_120110', '200310_130129', '200311_140046', '200312_140103',
                '200313_150123', '200314_160041', '200315_160059', '200316_170117',
                '200317_180037', '200318_180052', '200319_190111', '200320_210030',
                '200321_110039', '200322_120057', '200323_120116', '200324_130035',
                '200325_130052', '200326_140110', '200327_140027', '200328_150048',
                '200329_150102', '200330_160019', '200331_160037',
                '200401_160053', '200402_180012', '200403_200034', '200404_210052',
                '200405_110100',
                '200413_160113', '200414_040026', '200415_050039', '200416_050057',
                '200417_060019', '200418_080035', '200419_100053', '200420_110012',
                '200421_120028', '200422_120046', '200423_120003', '200424_130024',
                '200425_130038', '200426_135955']  # data that is used to display
n = len(columns_to_display) # no of z-heights displayed. this has to be an uneven numbe
r
n_row = 8
n_hor = int(n / n_row)          # calculate number of pictures on a row and make an int
eger of it
norm = plt.Normalize(-1,1)     # set range of 0 to 12 m height

fig, axes = plt.subplots(nrows=n_row, ncols=n_hor, figsize=(15, 45), sharey=True)  # ma
ke figure with subplots.
for i in range(n_row):
    for j in range(n_hor):
        index = j + i*n_hor                      # no. of the figure
        name1 = 'z_'+columns_to_display[index]    # first date name
        name2 = 'z_'+columns_to_display[index+1]  # second date name

        delta_z = data_grid[name2] - data_grid[name1]  # calculate difference in height
for the points

        pcm = axes[i, j].scatter(x=data_grid.x, y=data_grid.y , c=delta_z, s=1, cmap='c
oolwarm', norm=norm)  # plot data
        axes[i, j].set_title(name1[2:8] + '\n   to ' + name2[2:8])              # set
 figure titles, being the dates

fig.colorbar(pcm, ax=axes[:, :], location='right', shrink=0.6)             # colorbar o
n side
plt.show()
fig.savefig(filepath+'delta_z_all.png', bbox_inches = "tight");
```

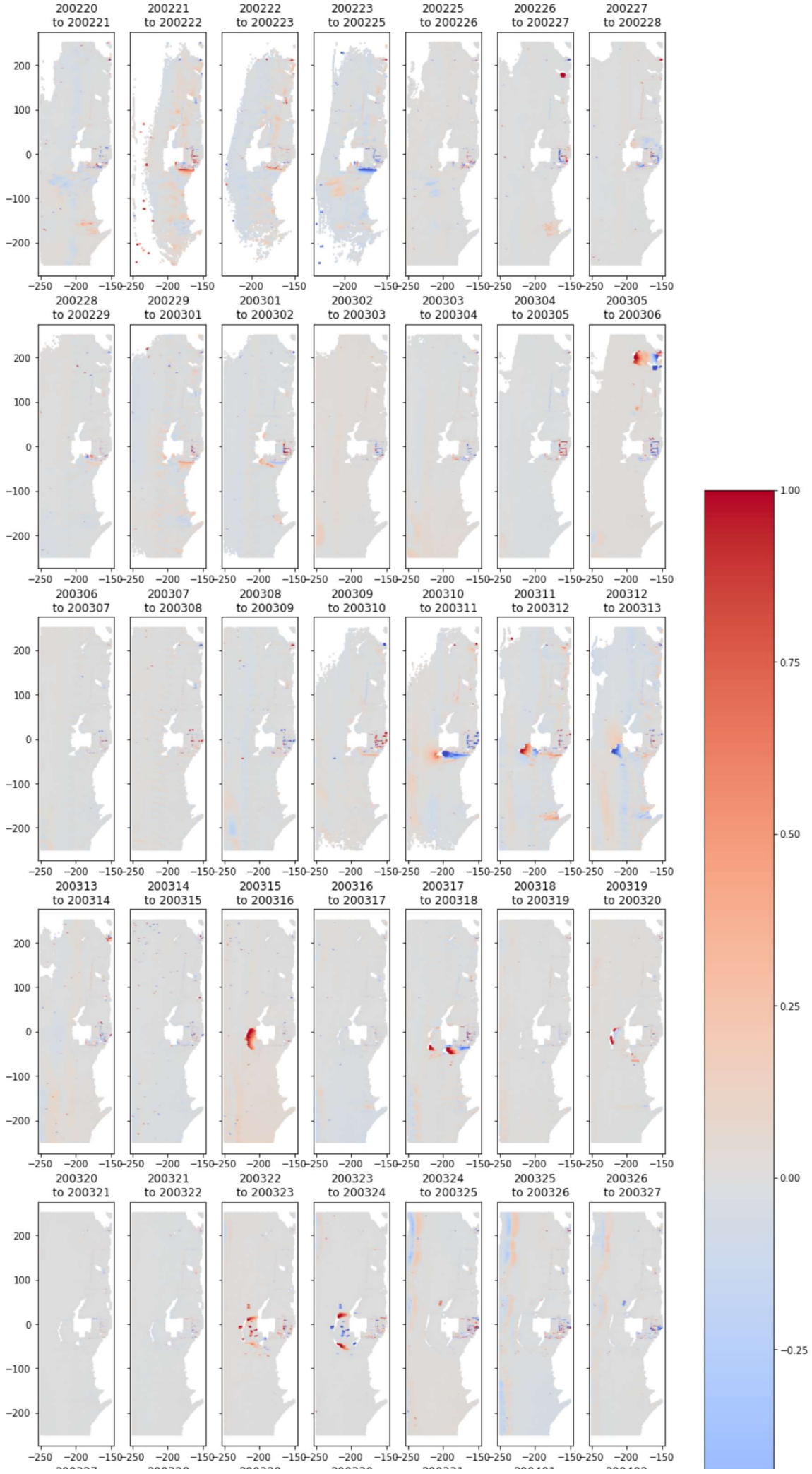
200220 to 200221
200221 to 200222
200222 to 200223
200223 to 200225
200225 to 200226
200226 to 200227
200227 to 200228
200228 to 200229
200229 to 200301
200301 to 200302
200302 to 200303
200303 to 200304
200304 to 200305
200305 to 200306
200306 to 200307
200307 to 200308
200308 to 200309
200309 to 200310
200310 to 200311
200311 to 200312
200312 to 200313
200313 to 200314
200314 to 200315
200315 to 200316
200316 to 200317
200317 to 200318
200318 to 200319
200319 to 200320
200320 to 200321
200321 to 200322
200322 to 200323
200323 to 200324
200324 to 200325
200325 to 200326
200326 to 200327
1.00
0.75
0.50
0.25
0.00
−0.25

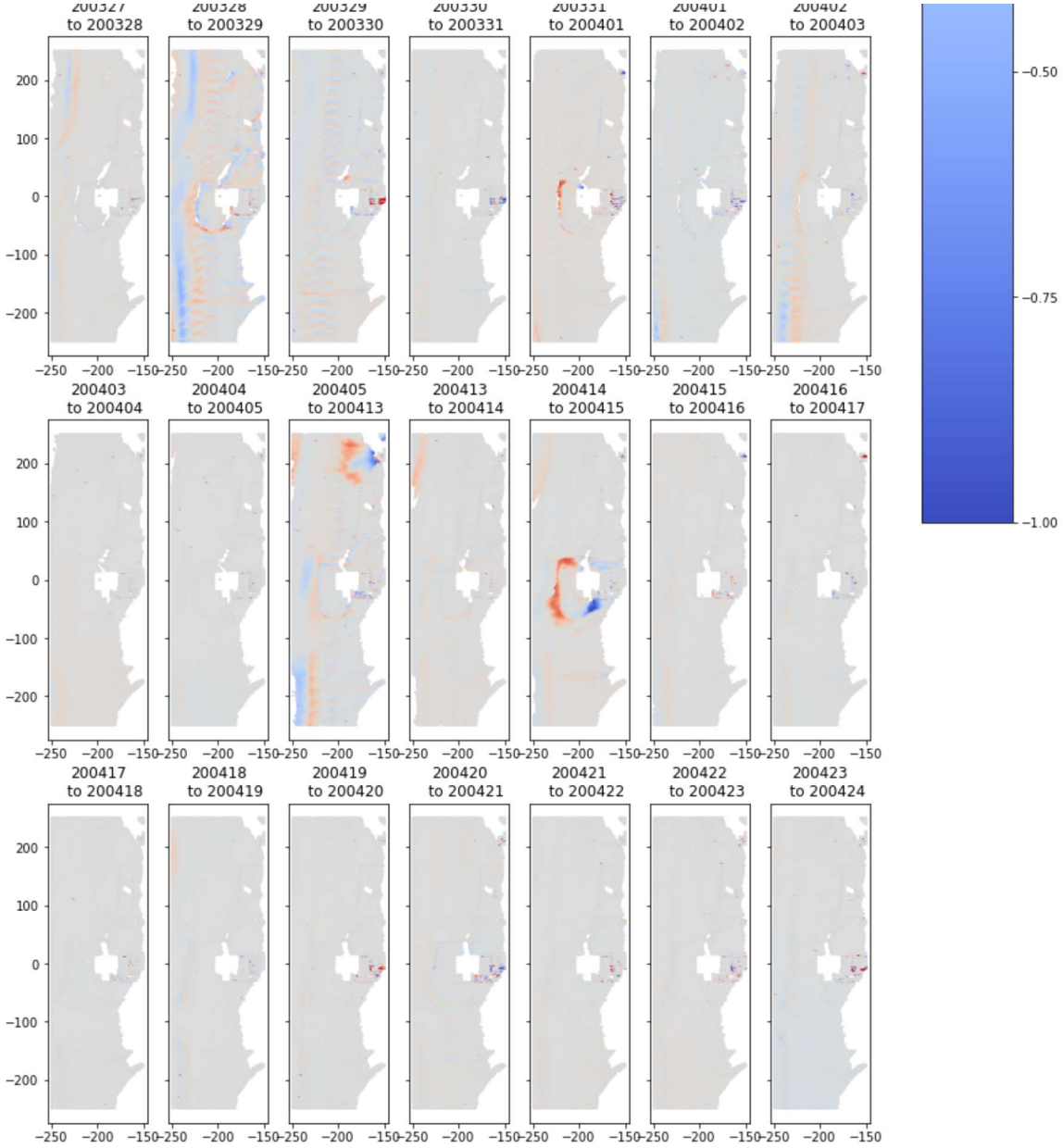
200327
to 200328
200328
to 200329
200329
to 200330
200330
to 200331
200331
to 200401
200401
to 200402
200402
to 200403
200403
to 200404
200404
to 200405
200405
to 200413
200413
to 200414
200414
to 200415
200415
to 200416
200416
to 200417
200417
to 200418
200418
to 200419
200419
to 200420
200420
to 200421
200421
to 200422
200422
to 200423
200423
to 200424
200
100
0
−100
−200
−250
−200
−150
−0.50
−0.75
−1.00

In [10]:

```
yet_to_do = [  ]
columns_displayed_and_saved = ['200220_100047', '200221_110109', '200222_120122', '2002
23_120041', #'200224_120059',]
                        '200225_130123', '200226_140138', '200227_150057',
                        '200228_150114', '200229_160131',
                        '200301_160050', '200302_150110', '200303_160126', '200304_1900
46',
                        '200305_200104', '200306_220124', '200307_230042', '200308_1100
51',
                        '200309_120110', '200310_130129', '200311_140046', '200312_1401
03',
                        '200313_150123', '200314_160041', '200315_160059', '200316_1701
17',
                        '200317_180037', '200318_180052', '200319_190111', '200320_2100
30',
                        '200321_110039', '200322_120057', '200323_120116', '200324_1300
35',
                        '200325_130052', '200326_140110', '200327_140027', '200328_1500
48',
                        '200329_150102', '200330_160019', '200331_160037',
                        '200401_160053', '200402_180012', '200403_200034', '200404_2100
52',
                        '200405_110100',
                        '200413_160113', '200414_040026', '200415_050039', '200416_0500
57',
                        '200417_060019', '200418_080035', '200419_100053', '200420_1100
12',
                        '200421_120028', '200422_120046', '200423_120003', '200424_1300
24' ]
columns_to_display = ['200425_130038', '200426_135955']  # the intervals between those
 are displayed and saved to a .png file
n = int(len(columns_to_display))
threshold = .2
norm = plt.Normalize(-1,1)     # to set scatterbar from -1 to 1 m height


for i in range(len(columns_to_display)-1):
        fig, axes = plt.subplots(1, 2, figsize=(10, 6),  gridspec_kw={'width_ratios': [
1, 3]})
        name1 = 'z_'+columns_to_display[i]    # first date name
        name2 = 'z_'+columns_to_display[i+1]  # second date name
        delta_z = data_grid[name2] - data_grid[name1]


        pcm = axes[0].scatter(x=data_grid.x, y=data_grid.y , c=delta_z, s=1, cmap='cool
warm', norm=norm)  # plot data
        axes[0].set_xlim([-250, -150])
        axes[0].set_ylim([-250, 250])

        delta_z = delta_z[~np.isnan(delta_z)]  # filter out Not a Number values
        z_left = delta_z[delta_z <= -threshold]
        z_mid = delta_z[(delta_z > -threshold) & (delta_z < threshold)]
        z_right = delta_z[delta_z >= threshold]

        bins = np.linspace(-4, 4, 161)
        axes[1].hist(z_left, bins=bins, color='mediumblue', label=f'$\Delta$z <= {-thre
shold}: {len(z_left)/len(delta_z)*100:.2f}% ')
        axes[1].hist(z_mid, bins=bins, color='grey', label=f'{-threshold} < $\Delta$z <
{threshold}: {len(z_mid)/len(delta_z)*100:.2f}% ')
```

```
        axes[1].hist(z_right, bins=bins, color='firebrick', label=f'$\Delta$z >= {thres
hold}: {len(z_right)/len(delta_z)*100:.2f}% ')
        axes[1].set_ylim([0, 100])
        axes[1].legend(loc="upper right")
        axes[1].set_xlabel('Height difference [m]')
        axes[1].set_ylabel('Number of grid cells')

        fig.colorbar(pcm, ax=axes[0], shrink=0.6)             # colorbar on side
        fig.suptitle(f'Height differences between {name1[2:]} and {name2[2:]}', y=1.02)
#, x=.45) # set figure titles, being the dates
        plt.tight_layout()
        plt.show()
        fig.savefig(filepath+name1[2:]+'_'+name2[2:]+'PointCloudAndHist.png', bbox_inch
es = "tight");
```

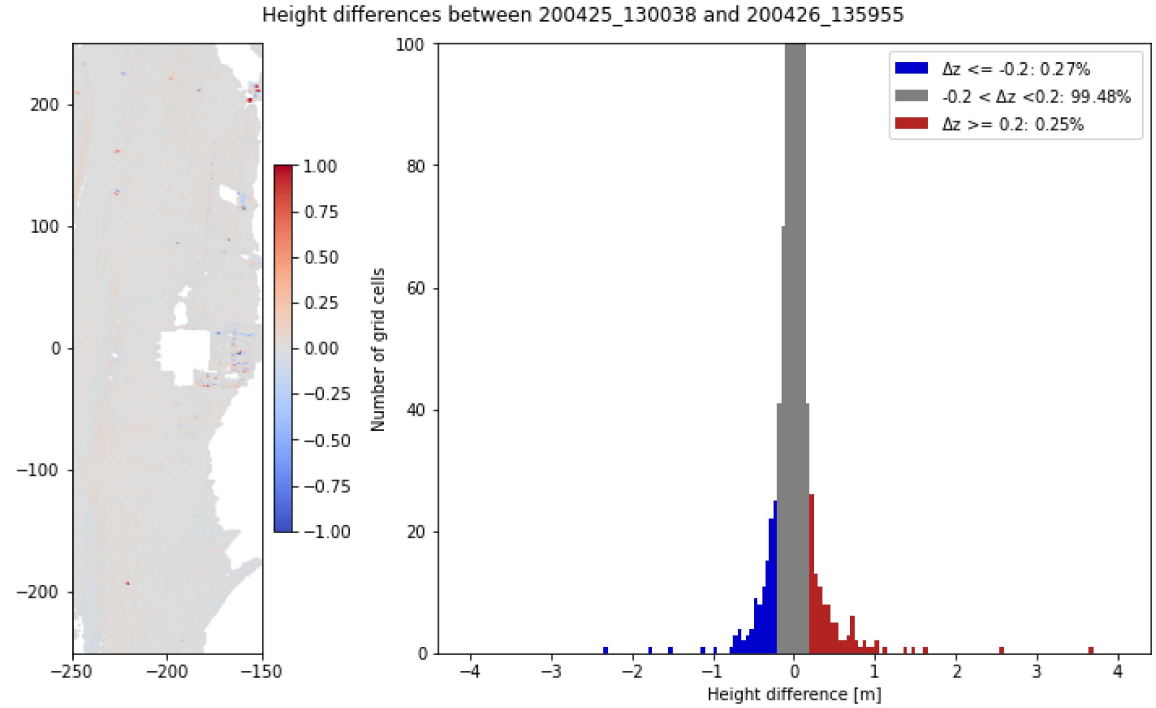

In [ ]: